A modified empirical mode decomposition method for multiperiod time-series detrending and the application in full-waveform induced polarization data

Journal Article

Author(s):
Liu, Weiqiang; Lü, Qingtian; Chen, Rujun; Lin, Pinrong; Chen, Chaojian (iD); Yang, Liangyong; Cai, Hongzhu

A modified empirical mode decomposition method for multiperiod time-series detrending and the application in full-waveform induced polarization data

Weiqiang Liu,[1] Qingtian Lü,[1] Rujun Chen,[2] Pinrong Lin,[3] Chaojian Chen,[2,4] Liangyong Yang[5] and Hongzhu Cai[6,7]

[1]*MNR Key Laboratory of Metallogeny and Mineral Assessment, Institute of Mineral Resources, CAGS, Beijing* 100037, *China. E-mail:* iccgcags@126.com
[2]*School of Geoscience and Info-physics, Central South University, Changsha, Hunan Province* 410083, *China*
[3]*MLR Laboratory of Geophysical EM Probing Technologies, Institute of Geophysical and Geochemical Exploration, Chinese Academy of Geological Sciences, Langfang, Hebei Province* 410083, *China*
[4]*Department of Earth Sciences, Institute of Geophysics, ETH Zurich,* 8092 *Zurich, Switzerland. E-mail:* chaojian.chen@outlook.com
[5]*Institute of Geology and Geophysics, Chinese Academy of Sciences (IGGCAS), Beijing* 100029, *China*
[6]*Department of Geoscience, Aarhus University, DK-*8000 *Aarhus C, Denmark*
[7]*Institute of Geophysics and Geomatics, China University of Geosciences (Wuhan), Wuhan* 430074, *China.*

SUMMARY

Trend drift is an annoying background interference in induced polarization (IP) exploration, which has great influence on the final calculation of apparent complex resistivity spectrum at low frequency (<0.1 Hz). This paper proposed a modified empirical mode decomposition (EMD) detrending technique for multiperiod IP data. The method uses local extreme values of the rising edges and the falling edges to form multiple envelopes and then to fit and eliminate the trend term. Through comparing with the traditional EMD methods using IP data with simulated trend drift, we find that the modified method can be used to obtain a more accurate fitting trend and the computational cost is only a fraction of that of the conventional one. Additionally, this detrending is little affected by other strong noise. We also used IP data with and without trend interferences to analyse this method, respectively. The results show that, for data without trend drift, the signals remain almost unchanged; however, for data with strong trend drift, the data quality is greatly improved and the calculation error is reduced. This technique is also applied to a large-scale multiperiod full-waveform IP data acquired in Zhegu Zn-Sb-Ag polymetallic deposit in southern Tibet, China. The apparent complex resistivity and phase of a survey line, a planar contour map and a pseudo-section with and without using the modified EMD were compared, respectively. Overall, before EMD detrending, the apparent phase results are rough and full of outliers. After detrending, the profiles are smooth and reasonable, and the outliers disappear. Both the results demonstrated that our proposed method can be adopted to effectively suppress trend drift interference without additional deviation in distributed full-waveform IP exploration.

Key words: Electrical resistivity tomography (ERT); Fourier analysis; Time-series analysis.

1 INTRODUCTION

Induced polarization (IP; Bleil 1953; Wait 1959; Zonge & Wynn 1975; He1997) is an effective electrical resistivity tomography (ERT) method for non-ferrous metallic mineral exploration (Xi *et al.* 2013; Mary *et al.* 2016; Tavakoli *et al.* 2016) and environmental investigations (Revil *et al.* 2015; Maurya *et al.* 2018; Power *et al.* 2018). Currently, there has been great development of IP in forward modelling (Karaoulis *et al.* 2013; Commer *et al.* 2017; Belliveau & Haber 2018; Qi *et al.* 2019), data acquisition (Eaton *et al.* 2010; Sun *et al.* 2012; Olsson *et al.* 2015; Mo *et al.* 2017), inversion and interpretation (Li & Oldenburg 2000; Fiandaca *et al.* 2018; Kim *et al.* 2018; Soueid *et al.* 2018; Zhdanov *et al.* 2018). However, electromagnetic (EM) interference is still a major limitation that restricts the further application of IP method, for instance, EM coupling, civilization interference, low-frequency trend interference and so on (Peter-Borie *et al.* 2011; Larsen *et al.* 2013; Li *et al.* 2017). EM coupling is caused by EM induction between the power supply line and the Earth, which is strong in high-frequency IP data and weak in low-frequency data and can be well removed in frequency domain (Dey & Morrison 1973; Johnson 1984; Routh & Oldenburg

2001; Zonge *et al.* 2005). Civilization interference is caused by industrial current interference, major power lines and other electric power equipment in survey area, which can be suppressed by time-series stacking, digital filtering and other nonlinear signal processing methods (Deo & Cull 2015; Olsson *et al.* 2016; Liu *et al.* 2016c; Liu *et al.* 2017). Apart from above-mentioned interferences, trend drift interference is also annoying in IP data, especially in low-frequency IP data (<0.1 Hz). This interference is mainly caused by telluric current, change of original electrode charge, spontaneous potential, zero drift of amplifier, variation of air temperature and other background low-frequency noises. Due to this interference, the observed potential signal in time domain will contain a trend drift with the time, and the calculated complex resistivity spectrum will be distorted after Fourier transformation. Several methods have been proposed in previous literatures for detrending. The polarization potentials on the potential electrodes can be corrected for by subtracting the polarization potential measured when no primary current and no IP signal are present (Dahlin *et al.* 2002). Additionally, the trend drift can be removed by fitting using a constant, linear or nonlinear mathematical model (Olsson *et al.* 2016). These methods are effective when the record of IP signal is short. However, when the signal series is long, and the trend drift is compounded by a variety of interference sources, it is difficult to fit the trend term drift with a specific mathematical function.

Empirical mode decomposition (EMD) is also an effective method for eliminating trend drift and does not require assumptions that trend terms satisfy some mathematical functions. After the proposal of the EMD method with the Hilbert Huang transform (HHT; Huang *et al.* 1998), several modified approaches are proposed to solve the mode aliasing effect caused by the common EMD, including ensemble EMD (EEMD; Wu & Huang 2009), complete ensemble EMD (CEEMD; Torres *et al.* 2011) and improved complete ensemble EMD (ICEEMD; Colominas *et al.* 2014). These methods have been widely used in geophysical data processing now, especially in seismic signal processing, including random noise reduction, coherent noise elimination, ground roll noise interference suppression, weak signal recognition, low-frequency information extraction, time-frequency analysis and so on (Battista *et al.* 2007; Bekara & Van der Baan 2009; Chen *et al.* 2010; Han & Baan 2013; Chen & Ma 2014; Xue *et al.* 2014; Chen *et al.* 2015; Han & van der Baan 2015; Chen 2016; Chen *et al.* 2016; Chen *et al.* 2017a,b). EMD and Hilbert–Huang transform are also applied to non-seismic data processing. In microgravity signal processing, EMD based analysis methods for the gravimeter records can improve signal-to-noise ratio (SNR) and extract gravity anomalies (Hassan 2005; Huang *et al.* 2010; Shen & Ding 2014). In geomagnetic signal processing, the EMD method is used to analyse the records of globally distributed geomagnetic field to study the effects of core fluid dynamics (Jackson & Mound 2010). In EM signal processing, EMD and HHT are applied to process very low frequency EM (VLF-EM) and magnetotelluric data to obtain a more stable impedance estimation (Jeng *et al.* 2007; Cai *et al.* 2009; Chen *et al.* 2012).

In recent years, many other new signal processing methods have been proposed and applied in geophysical data detrending and time-frequency analysis, including mathematical morphological filtering (MMF; Serra 1986), empirical wavelet transform (EWT; Gilles 2013), variational mode decomposition (VMD; Dragomiretskiy & Zosso 2014), EMD-seislet transform (Chen & Fomel 2017) and so on. MMF is an automatic pattern recognition method with high efficiency, which has been used in magnetotelluric and microseismic signal processing (Li *et al.* 2016; Huang *et al.* 2017). For MMF, determining an optimal function and dimensions of structural elements is necessary. Variational modal decomposition is insensitive to random noise and can reduce redundant components (Liu *et al.* 2016a). EWT is an adaptive signal-analysis approach like the EMD with a consolidated mathematical theory (Liu *et al.* 2016b). Now, both VMD and EWT are mainly used for time-frequency analysis of signals. Their application in multiperiod series detrending needs to be further studied. EMD-seislet transform combined the 1-D non-stationary seislet transform with EMD in the f–x domain, which has been used for sparsity-promoting seismic data processing but requires large computational cost (Chen & Fomel 2017).

In the above researches, the EMD, improved EMD and other new methods are mainly used in the long-period stochastic signal processing, such as microgravity, magnetotelluric and seismic signal. No one has yet applied these methods to multiperiod regular signal detrending, such as: full waveform direct current signal, IP signal, etc. Although the EMD method has been developed and completed, it still faces the problem of large computation. In this paper, we proposed a modified EMD method for multiperiod time detrending. Through comparison with traditional EMD methods, we found that the modified method can avoid incomplete detrending and damage of useful signal. In addition, the computational cost is only a fraction of that of the conventional EMD methods. By applying this method to large-scale practical IP data, the quality of complex resistivity spectrum is greatly improved.

2 FULL-WAVEFORM INDUCED POLARIZATION DATA

Nowadays, several distributed full-waveform IP instrument systems are developed, such as Newmont distributed IP data acquisition system (Eaton *et al.* 2010; Sun *et al.* 2012), Quantec's 3-D system (Gharibi *et al.* 2012), IRIS instrument (Gourry *et al.* 2003) and the distributed spread spectrum IP system (SSIP; Chen *et al.* 2007; Xi *et al.* 2013; Xi *et al.* 2014). There are two advantages by using these distributed instruments for electrical prospecting. The first one is that the work efficiency is improved by multichannel synchronous acquisition and the other is that the multiperiod full-waveform current and voltage data are recorded, which are more suitable for the anti-interference processing. Compared with traditional ERT methods, the method using distributed full-waveform acquisition has a larger detection depth and a larger data volume. In this paper, we use the IP data acquired by distributed SSIP to test the signal processing method for removing low-frequency trend interference.

In spread spectrum IP exploration, the transmitter can transmit various waveforms, including pseudo-random *m*-sequence, pseudo-random 2^n-sequence, rectangular wave and other combined waves. The frequency ranges from 1/256 to 128 Hz, which is spread and suitable
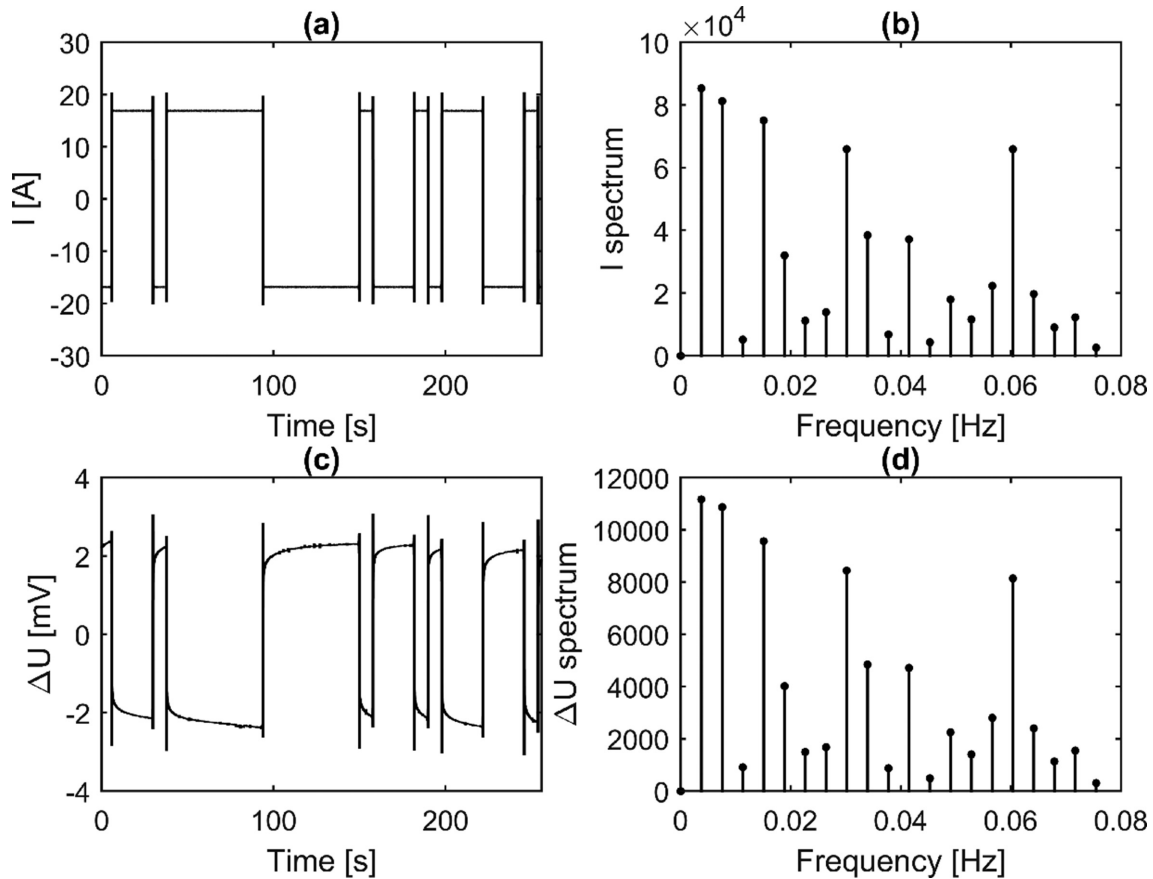
Figure 1. (a) Supplying current signal in one period; (b) frequency spectrum of the supplying current (five basic frequencies show greater amplitude); (c) synchronous IP potential difference signal in one period; (d) frequency spectrum of the synchronous potential difference (five basic frequencies show greater amplitude).

for frequency-domain IP exploration. A pseudo-random sequence is a binary sequence that exhibits statistical behaviour like a truly random sequence. In the time domain, the values of 0 and 1 occur randomly, and in the frequency domain, the signal energy is uniformly distributed across multiple frequencies. Generally, two kinds of pseudo-random signals are used in IP electrical prospecting, including pseudo-random *m*-sequence (Golomb 1982) and pseudo-random 2^n-sequence (He *et al.* 2015). In time domain, combinations of multiple rectangular waves of different widths are used. In frequency domain, the energy of the *m*-sequence is uniformly distributed on multiple frequencies with linear intervals, such as f_0, f_0*2, f_0*3, f_0*4, etc., and the energy of the 2^n-sequence is uniformly distributed on multiple frequencies with logarithmic interval, such as $f_0, f_0*2^1, f_0*2^2, f_0*2^3, f_0*2^4$ Hz, etc., where f_0 is the fundamental frequency. The above two sequences are suitable for EM sounding and spectral IP exploration. The complex resistivity of multiple frequencies can be calculated simultaneously through one emission, so the efficiency of the field work can be significantly improved.

Aiming to detect the concealed Pb-Zn deposit, SSIP data were acquired in Zhegu Zn-Sb-Ag polymetallic deposit in southern Tibet of southwest of China. 10 survey lines (about 300 survey points in total) were arranged using non-conventional sweeping and sounding array protocol. Transmitting current is a 2^5 pseudo-random sequence. In time domain, the sampling rate is 64 Hz and the period is 256 s. In frequency domain, the fundamental frequency f_0 is 1/265 Hz and energies of this sequence are mainly distributed in 1/256, 2/256, 4/256, 8/256 and 16/256 Hz. The complex resistivity is calculated at the five main frequencies. Figs 1(a) and (c) show the transmitting current and acquired potential difference signal of one period. Figs 1(b) and (d) show part of the frequency spectrum of current and potential difference. From Fig. 1, we can see that the energies of current and potential are mainly distributed in 1/265 Hz (0.0039 Hz), 2/265 Hz (0.0078 Hz), 4/265 Hz (0.0156 Hz), 8/265 Hz (0.0313 Hz) and 16/265 Hz (0.0625 Hz).

Because the frequency of IP signal is low, the spectrum of EM coupling can be ignored, and the complex resistivity is calculated using the following formula:

$$\rho(f) = K \frac{U(f)}{I(f)}, \tag{1}$$

where, $U(f)$ is the frequency spectrum of potential difference data, and $I(f)$ is the frequency spectrum of synchronous current data, which are calculated using fast Fourier transform (Oppenheim 1989). K is the array coefficient given by

$$K = 2\pi \frac{1}{\left(\dfrac{1}{AM} - \dfrac{1}{BM}\right) - \left(\dfrac{1}{AN} - \dfrac{1}{BN}\right)},$$ (2)

where A and B are current electrodes, M and N are potential electrodes. AM, BM, AN, BN are electrode spaces (Bhattacharya & Patra 1968). In this study, the apparent complex resistivities of five basic frequencies are calculated.

3 A MODIFIED EMPIRICAL MODE DECOMPOSITION FOR DETRENDING OF MULTIPERIOD TIME-SERIES

3.1 A modified empirical mode decomposition method

EMD was first proposed by Huang *et al.* (1998). Then, some advanced methods were proposed, such as EEMD, CEEMD and ICEEMD (Wu & Huang 2009; Torres *et al.* 2011; Colominas *et al.* 2014), in which the model mixing problem and the residual random noise problem are further solved. The conventional EMD method divides the original signal $S(t)$ into a series of intrinsic mode components $c_k(t)_{k=1 \sim n}$ and a residue $r(t)$, namely,

$$S(t) = \sum_{k=1}^{n} c_k(t) + r(t).$$ (3)

The residue, $r(t)$, is a monotonic function. The EEMD method adds a variety of Gaussian white noises to the original signal to obtain multiple groups of intrinsic mode functions (IMF) estimates, and then averages them to reduce the mode aliasing. However, residual noise may still exist. The CEEMD method adds particular noises instead of rand noises at each stage of the decomposition to obtain each mode with little noise. The ICEEMD was further proposed to obtain less noises in each IMF estimate and to reduce the occurrence of spurious IMFs.

For the above methods, there are usually two ways to distinguish and extract trend terms. First, the residue $r(t)$ is regarded as the trend term, and the data without trend term are obtained by summing all intrinsic mode components. Second, sum of the residue and last few intrinsic mode components is taken as the trend term, the data without trend term are obtained by summing only the left intrinsic modal components (Flandrin *et al.* 2004). However, still some problems exist in applying the above methods to the time-series detrending. Incomplete detrending or loss of useful signals may be caused as it is difficult to determine which components are the real trend term. For multiperiod IP data, due to the complexity of the signal itself, both IP information and trend terms exist in all the intrinsic modal components. Adopting the residue as the trend will result in incomplete detrending, while adopting sum of the residue and last few IMFs as the trend will cause serious loss to the IP signal. In addition, the above methods require high computational costs, which means that it is time-consuming if they are applied to detrend large-scale data sets.

To reduce the distortion caused by the detrending algorithm itself, here, we propose a modified EMD method to detrend multiperiod signal, such as square wave sequence, pseudo-random wave sequence, etc. For a multiperiod signal $S(t)$ with the period being T, there may be several local intrinsic maxima $A_1, A_2, ..., A_{n_1}$ and minima $B_1, B_2, ..., B_{n_2}$ within a period. The local extreme points at different positions in a period may not be equal, namely, $A_1 \neq A_2 \neq ... A_{n_1}$ and $B_1 \neq B_2 \neq ... B_{n_2}$. However, the extreme points at the same position in different periods should be equal when the signal is not disturbed by the trend drift and noise interference, namely,

$$\begin{cases} A_1(t_1+kT)=A_1(t_1) \\ A_2(t_2+kT)=A_2(t_2) \\ ... \\ A_{n_1}(t_{n_1}+kT)=A_{n_1}(t_{n_1}) \end{cases} \text{and} \begin{cases} B_1(t_1+kT)=B_1(t_1) \\ B_2(t_2+kT)=B_2(t_2) \\ ... \\ B_{n_2}(t_{n_2}+kT)=B_{n_2}(t_{n_2}) \end{cases}.$$ (4)

When the original signal contains trend drift interference, the above formula (4) does not hold. The proposed modified EMD method using the extreme points of all the periods is used to fit the trend. First, we construct upper and lower envelopes successively. $A_1(t_1), A_1(t_1 + T), A_1(t_1 + 2T), A_1(t_1 + 3T), \ldots, A_1(t_1 + kT)$ are used to construct an upper envelope $U_1(t)$ covering all the data by interpolation. $B_1(t_1), B_1(t_1 + T), B_1(t_1 + 2T), B_1(t_1 + 3T), \ldots, B_1(t_1 + kT)$ are used to construct a lower envelope $L_1(t)$. By analogy, all the maxima $A_2, ..., A_{n_1}$ and minima $B_2, ..., B_{n_2}$ are used to form envelopes, namely,

$$\begin{cases} U_1(t) = interp([t_1, t_1 + T, ..., t_1 + kT], [A_1(t_1), A_1(t_1 + T), ..., A_1(t_1 + kT)], t) \\ U_2(t) = interp([t_2, t_2 + T, ..., t_2 + kT], [A_2(t_2), A_2(t_2 + T), ..., A_2(t_2 + kT)], t) \\ ... \\ U_{n_1}(t) = interp([t_{n_1}, t_{n_1} + T, ..., t_{n_1} + kT], [A_{n_1}(t_{n_1}), A_{n_1}(t_{n_1} + T), ..., A_{n_1}(t_{n_1} + kT)], t) \end{cases},$$ (5)
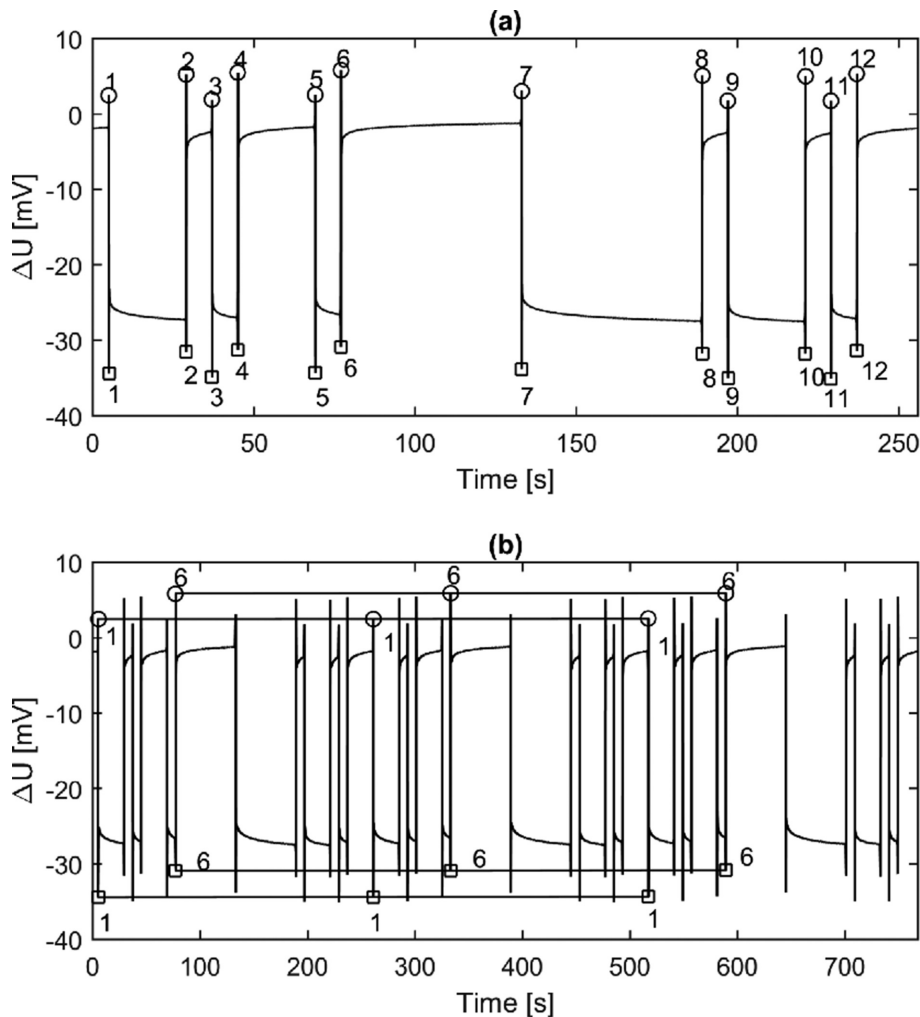
Figure 2. (a) The IP potential data of one period when the transmitted current is a pseudo-random wave (there are 12 maxima and 12 minima, but they're not equal even though there's no trend interference); (b) the IP potential data of three period (the extreme points at the same position in different periods are equal when there's no trend interference).

and

$$
\begin{cases}
L_1(t) = interp([t_1, t_1 + T, ..., t_1 + kT], [B_1(t_1), B_1(t_1 + T), ..., B_1(t_1 + kT)], t) \\
L_2(t) = interp([t_2, t_2 + T, ..., t_2 + kT], [B_2(t_2), B_2(t_2 + T), ..., B_2(t_2 + kT)], t) \\
... \\
L_{n_2}(t) = interp([t_{n_2}, t_{n_2} + T, ..., t_{n_2} + kT], [B_{n_2}(t_{n_2}), B_{n_2}(t_{n_2} + T), ..., B_{n_2}(t_{n_2} + kT)], t)
\end{cases}
\tag{6}
$$

All above interpolations use cubic spline interpolation method as in Huang *et al.* (1998). Finally, multiple upper envelopes $U_1(t), U_2(t)$, ... , $U_{n_1}(t)$ and lower envelopes $L_1(t), L_2(t), ... , L_{n_2}(t)$ are obtained. Then all the envelopes are stacked to get the first-order trend $h_1(t)$,

$$
h_1(t) = \frac{1}{n_1} \sum_{i=1}^{n_1} U_i(t) + \frac{1}{n_2} \sum_{i=1}^{n_2} L_i(t),
\tag{7}
$$

and, $h_1(t)$ is separated from the original data by

$$
s_1(t) = S(t) - h_1(t).
\tag{8}
$$

Since the residue $s_1(t)$ may still contain trend variations, it is furtherly treated as the new data $S(t)$ and recursively subjected to the same processing as the above formulae (5)–(8) until the difference between the *m*th residue $h_m(t)$ and the 0-value line is less than a given threshold.
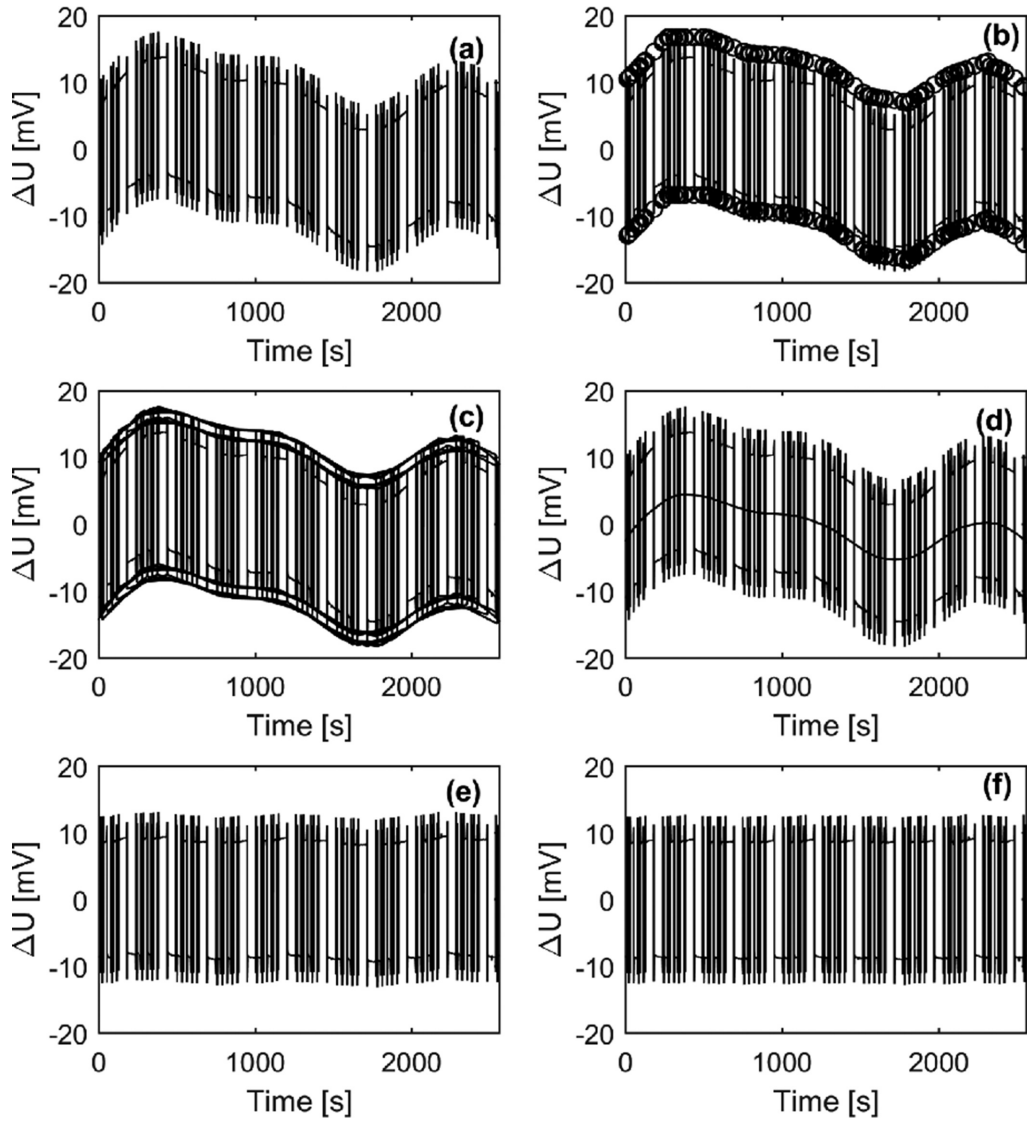
Figure 3. Using modified empirical mode decomposition (EMD) method to remove the trend drift of the IP signal. (a) The original sequence, (b) the local maxima and minima, (c) the multiple upper and lower envelopes, (d) the fitting trend term, (e) the signal after detrending and (f) the final IP signal obtained by repeating the above process (a)-(e).

The above detrending process can be represented by a formula:

$$
\begin{aligned}
S(t) &= s_1(t) + h_1(t) \\
&= s_2(t) + h_2(t) + h_1(t) \\
&= s_3(t) + h_3(t) + h_2(t) + h_1(t) \\
&\ldots\ldots \\
&= s_m(t) + h_m(t) + h_{m-1}(t) + \ldots\ldots + h_1(t) \\
&= s_m(t) + \sum_{i=1}^{m} h_i(t)
\end{aligned}
\tag{9}
$$

where $s_m(t)$ is the filtered signal without trend drifts. All the extreme points in different periods at the same position of the $s_m(t)$ are equal, and formula (4) will be satisfied approximatively. The $\sum_{i=1}^{m} h_i(t)$ is the fitting trend.

The whole process of the modified EMD is like the calculation of an IMF in the traditional EMD method, but the envelope formation methods are different. Traditional EMD interpolates all extremum to form an envelope. The modified method uses the extreme points of many groups to form multiple envelopes. Now, we use a pseudo-random combined square wave IP signals to show these. Fig. 2(a) shows the IP potential data of one period, there are 12 local maxima and 12 local minima in a period, which are not equal. Fig. 2(b) shows the IP potential data of three periods. We use the extreme points in a same position of all the three periods to construct an upper or lower envelope. 12 upper envelopes and 12 lower envelopes can be obtained (only two were plotted in the figure). Subsequently, we calculated the mean value $h_1(t)$ of
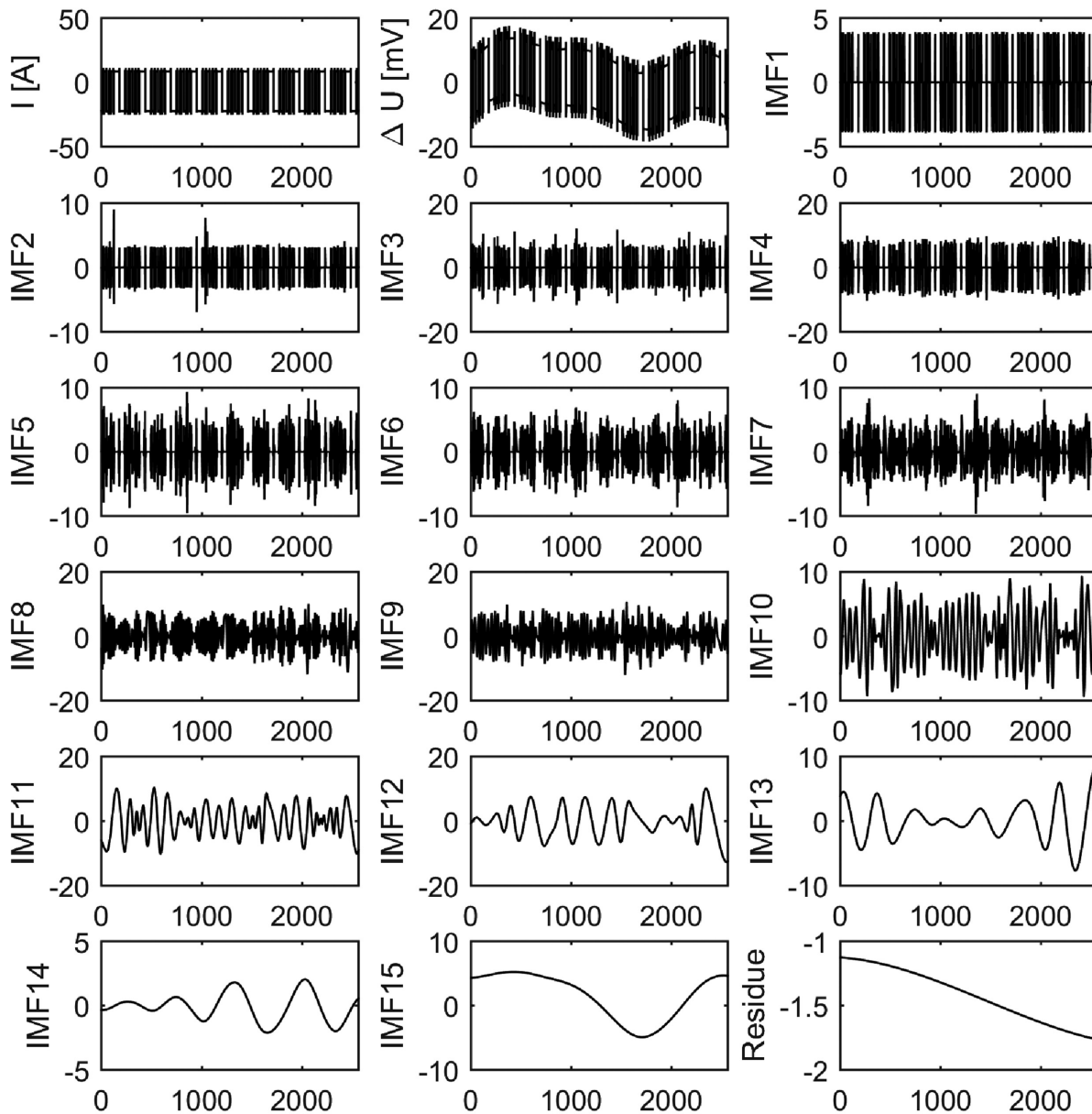
Figure 4. Using the empirical mode decomposition (EMD) method to decompose the IP potential difference data signal. [The subplots are transmitted current data, observed voltage data contaminated by trend drift interference, all the IMFs and the residue in turn, the *x*-coordinate is time (s) and the *y*-coordinate is amplitude (mV)].

all the 12 upper and 12 lower envelopes and subtract the mean $h_1(t)$ from the original series. Assume the difference is the first components $s_1(t)$. After several iterations using formula (9), the trend term and the filtered IP signal are obtained. Finally, all the extreme points satisfy formula (4).

For common multiperiod signals, the location of local extremum is uncertain. However, for IP signal of rectangular waveform, the local maxima and minima are located in rising and falling edges, such as the voltage spikes in Fig. 2(a). The origin of voltage spikes at the current switches is an EM effect. These spikes arise from inductive interactions between conductive near-surface ground and the wires carrying transmitter current. When current switches, secondary currents generated by the Earth's EM induction cause the observed potential to peak, and the induced secondary current rapidly decays as the primary current is stationary (Nabighian & Macnae 1991). The form of EM effect on the measured data is similar regardless of which waveform is supplied. According to the EM induction law, EM effect is mainly shown in the rising and falling edges of current mutation. It is represented by the sharp pulse of the voltage signal with large amplitude and fast attenuation. When a different current waveform (rectangular wave, bipolar wave, *m*-sequence wave, 2^n-sequence wave, etc.) is used, the number of local extremities in a period may change, but the extremities remain in rising and falling edges.
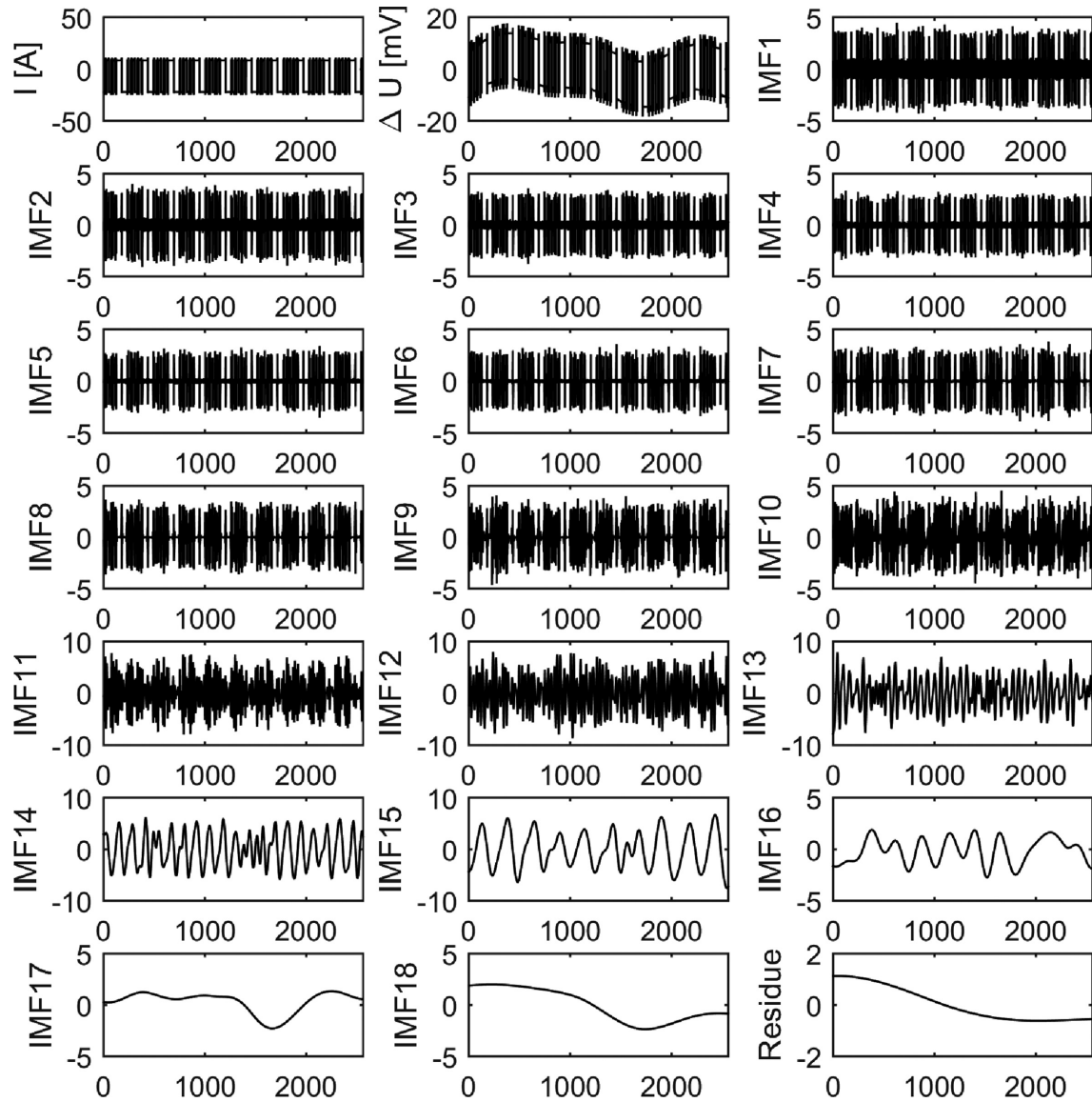
Figure 5. Using the ensemble empirical mode decomposition (EEMD) method to decompose the IP potential difference data signal. [The subplots are transmitted current data, observed IP voltage data contaminated by trend drift interference, all the IMFs and the residue in turn, the *x*-coordinate is time (s) and the *y*-coordinate is amplitude (mV)].

Although the EM effect is affected by a variety of factors including earth resistivity, observation device, instrument system response, etc., for multiperiod IP signal, EM effect of different periods at the same position should be equal as shown in formula (4), when there is no tend drift and noise interference. Since local maxima and local minima within a period may be affected by noise practically, using only one envelope to fit the trend will lead to distortion. Using the average of multiple envelopes can suppress the influence of noise interference on the trend line estimate. In Section 3.2, the detrending effects in the background of strong interference are illustrated with examples.

3.2 Comparison with conventional empirical mode decomposition methods

We use three data sets to compare the detrending effects of the proposed modified EMD method, the traditional EMD, EEMD, CEEMD and ICEEMD. The standard IP data was collected in a high SNR area with no trend item interference. The first data set is the IP signal that is disturbed by a simulated sinusoidal trend $\text{trend}_1(t)$. The second one is the IP voltage data without trend-term interference, namely, $\text{trend}_2(t) = 0$. The third one is the IP voltage data contaminated by trend drift $\text{trend}_1(t)$, background noise and burst noise interference. Expressions of these three simulated trends are:

$$\text{trend}_1(t) = 2\sin(2\pi f_1 t) + 2\sin(2\pi f_2 t) + \sin(2\pi f_3 t)$$
$$f_1 = 1/4000, \ f_2 = 1/2000, \ f_3 = 1/1000, \ t = 0 : 0.0156 : 2560s, \tag{10}$$
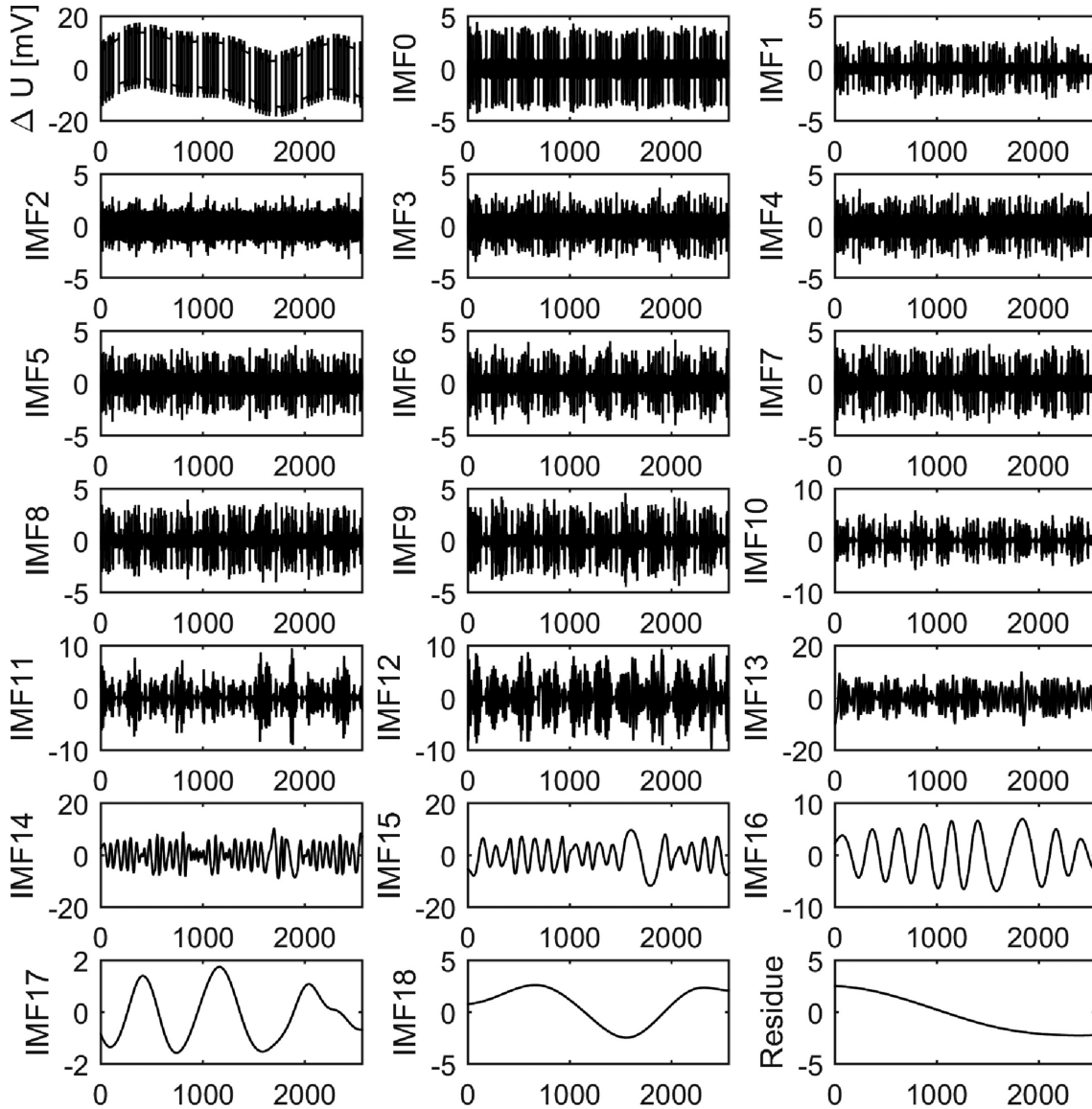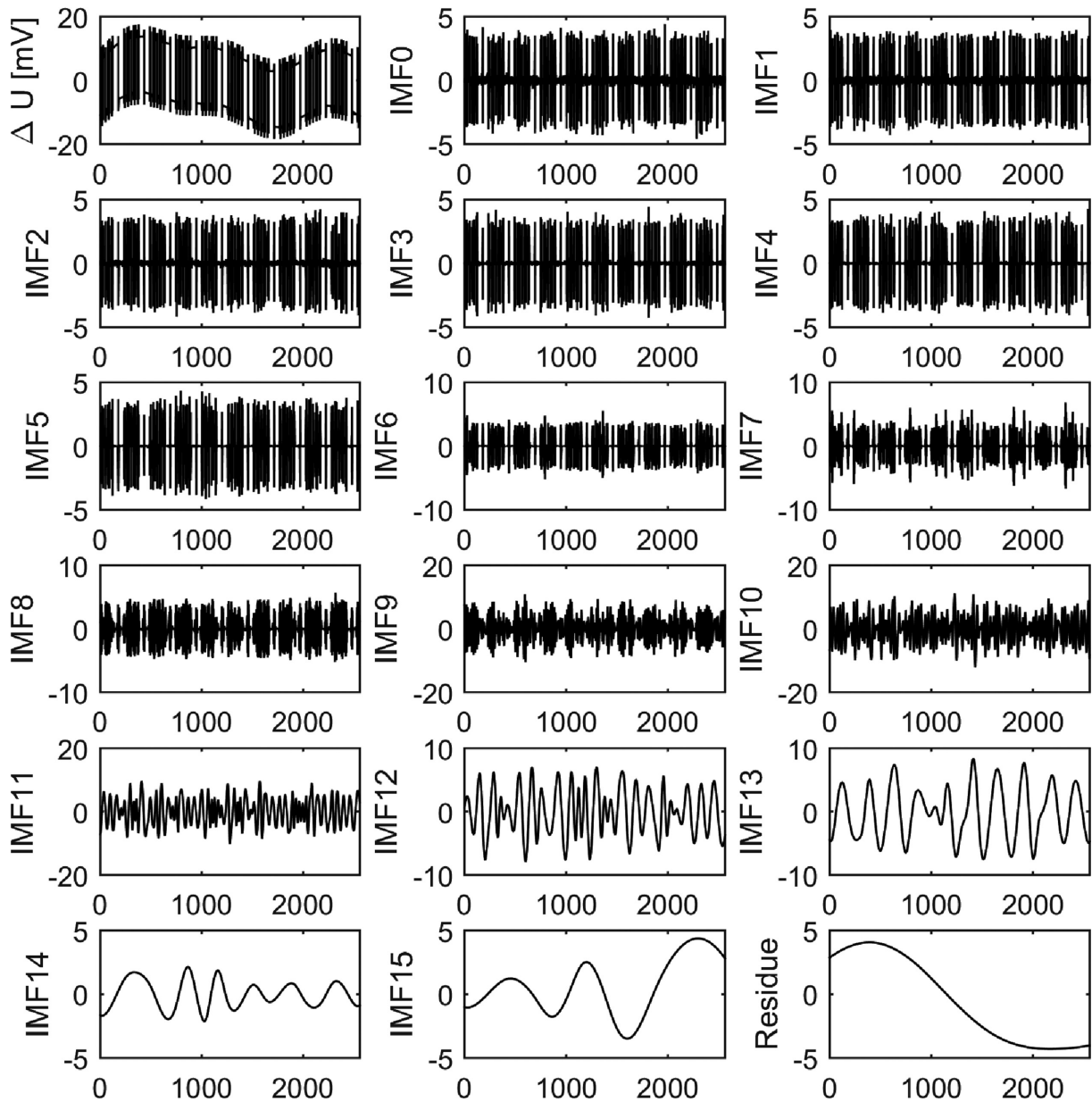
Figure 6. Using the complete ensemble empirical mode decomposition (CEEMD) method to decompose the IP potential difference data signal. (The subplots are observed IP voltage data contaminated by trend drift interference, all the IMFs and the residue in turn, the *x*-coordinate is time (s) and the *y*-coordinate is amplitude (mV)).

$$\text{trend}_2(t) = 0$$
$$t = 0 : 0.0156 : 2560s, \tag{11}$$

$$\text{trend}_3(t) = \text{trend}_1(t) + \text{Random noise} + \text{impulse noise}$$
$$t = 0 : 0.0156 : 2560s. \tag{12}$$

First, we use the proposed modified EMD method to deal with the first data set (Model 1 in Table 1). Fig. 3(a) shows the original sequence, Fig. 3(b) shows the local maxima and minima, Fig. 3(c) shows the multiple upper and lower envelopes, Fig. 3(d) shows the fitting trend term, Fig. 3(e) shows the signal after detrending. Then, it is treated as the new signal, and subjected to the same processing as shown in Figs 3(a)–(e). The total number of iterations is approximately the number of iterations needed to solve an IMF in conventional EMD. Finally, a pure signal without trend drifting is obtained in Fig. 3(f). The difference between the original signal and the obtained signal is the fitting trend term, and the comparison with the real trend term is shown in Fig. 8(a). Then, we use conventional EMD methods to process the contaminated signal. All the above methods decompose the original signal $S(t)$ into a series of intrinsic mode components (IMFs) and a residue. Figs 4–7 show the decomposition results using EMD, EEMD, CEEMD, and ICEEMD, respectively.

Figure 7. Using the improved ensemble empirical mode decomposition (ICEEMD) method to decompose the IP potential difference data signal. [The subplots are transmitted current data, observed IP voltage data contaminated by trend drift interference, all the IMFs and the residue in turn, the *x*-coordinate is time (s) and the *y*-coordinate is amplitude (mV)].

We use the residue or the sum of the residue and last several IMFs to fit trend drift. Fig. 8 shows the comparison of the real trend and the fitted trends for all the methods, where, the solid line is the real trend term, and the dotted line is the calculated trend term. Figs 8(a1)–(a4) look the same, representing the trend obtained by the modified EMD method and the real trend term, which have completely overlapped. Figs 8(b1)–(b4) show the fitting trends using the EMD method. In Fig. 8(b1), the dotted line is the residue; in Fig. 8(b2), the dotted line is the sum of the residue and the last IMFs; in Fig. 8(b3), the dotted line is the sum of the residue and the last two IMFs; in Fig. 8(b4), the dotted line is the sum of the residue and the last three IMFs. Figs 8(c1)–(c4) show the fitting trends using the EEMD method, Figs 8(d1)–(d4) show the fitting trends using the CEEMD method, Figs 8(e1)–(e4) show the fitting trends using the ICEEMD method, and the subfigures in each column represent the sum of the different components.

From Fig. 8, we can find that taking the residue as a trend term will result in incomplete fitting (such as Figs 8a1–e1), while taking the sum of the residue and the last three IMFs will lead to overfitting (such as Figs 8a4–e4), which results in a loss of useful signals. For the EMD and ICEEMD methods, taking the sum of the residue and the last component as the trend term will obtain the best effect (see Figs 8b2 and e2). For the EEMD and CEEMD methods, taking the sum of the residue and the last two components as the trend term will obtain the best effect (see Figs 8c3 and d3). However, the best fitting effects of the conventional methods are not as good as that of the modified EMD method.
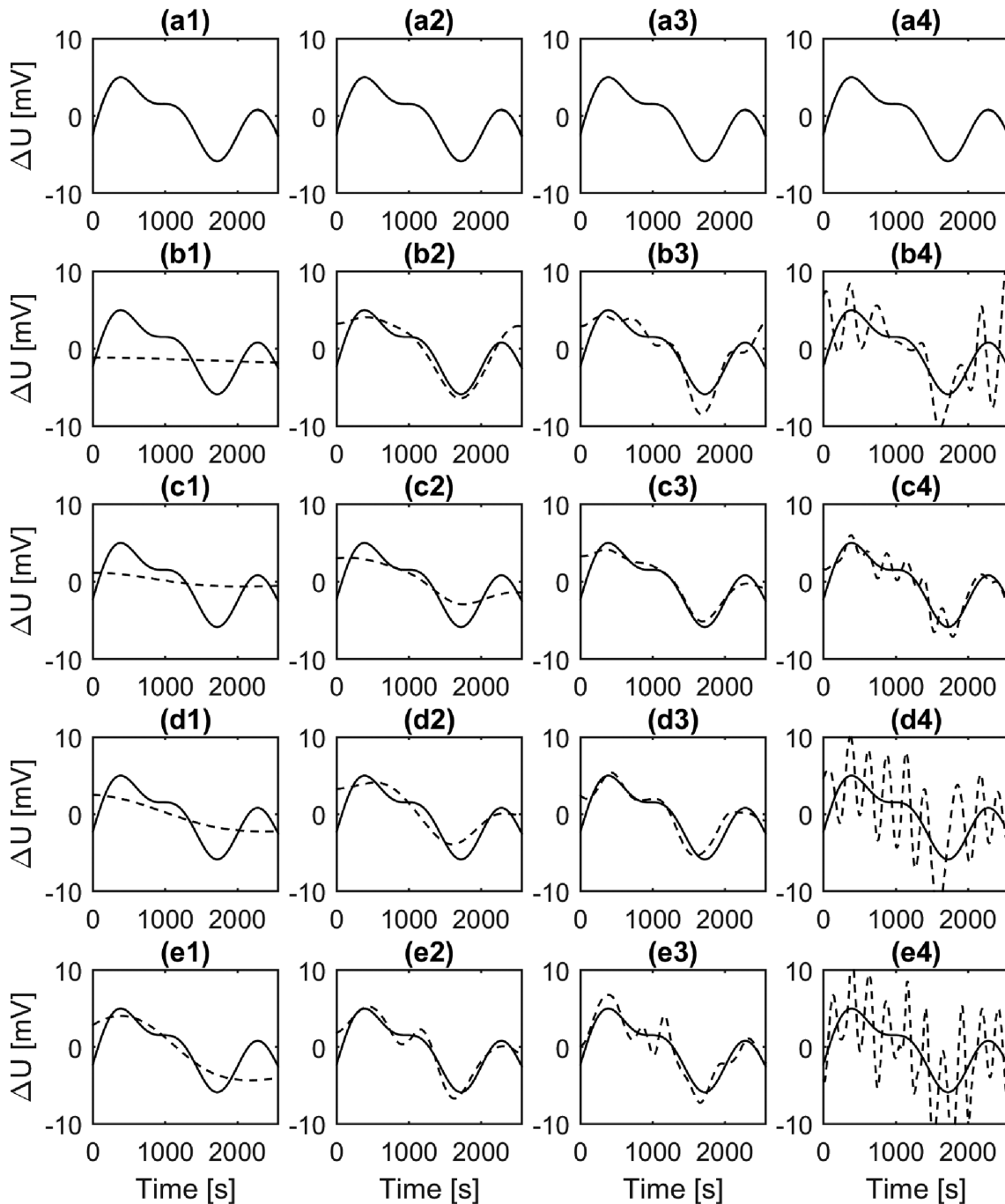
Figure 8. Comparisons of the real trend (solid line) and the fitting trend (dotted line) using different methods when the original data are contaminated by sinusoidal trend drift interference. (a1)–(a4) show the same figure, representing the trend obtained by the modified EMD method (dotted line) and the real trend term (solid line), which have completely overlapped. (b1)–(b4) show the fitting trends using the EMD method: in (b1), the dotted line is the residue; in (b2), the dotted line is the sum of the residue and the last IMF; in (b3), the dotted line is the sum of the residue and the last two IMFs; in (b4), the dotted line is the sum of the residue and the last three IMFs. (c1)–(c4) show the fitting trends using the EEMD method, (d1)–(d4) show the fitting trends using the CEEMD method, and (e1)–(e4) show the fitting trends using the ICEEMD method.

Next, we use another two data sets (Model 2 and model 3 in Table 1) to analyse the detrending effect of different methods, including IP voltage data without trend-term interference and IP data containing trend drift, background noise and burst noise interference. In order to save space, only trend fitting results are shown below, and the empirical modal components and residuals obtained by decomposition are not shown here. Fig. 9 shows the comparison of the real trend and the fitted trends using different methods, when the observed IP voltage data are not contaminated by trend drift interference. From Figs 9(a1)–(a4), when the original signal does not contain the trend-term interference, the fitting result is a 0 value curve using the proposed method. From Figs 9(b)–(e), all the fitting results of the conventional methods are biased. Fig. 10 shows the comparison of the real trend and the fitted trends using different methods, when the observed IP voltage data are
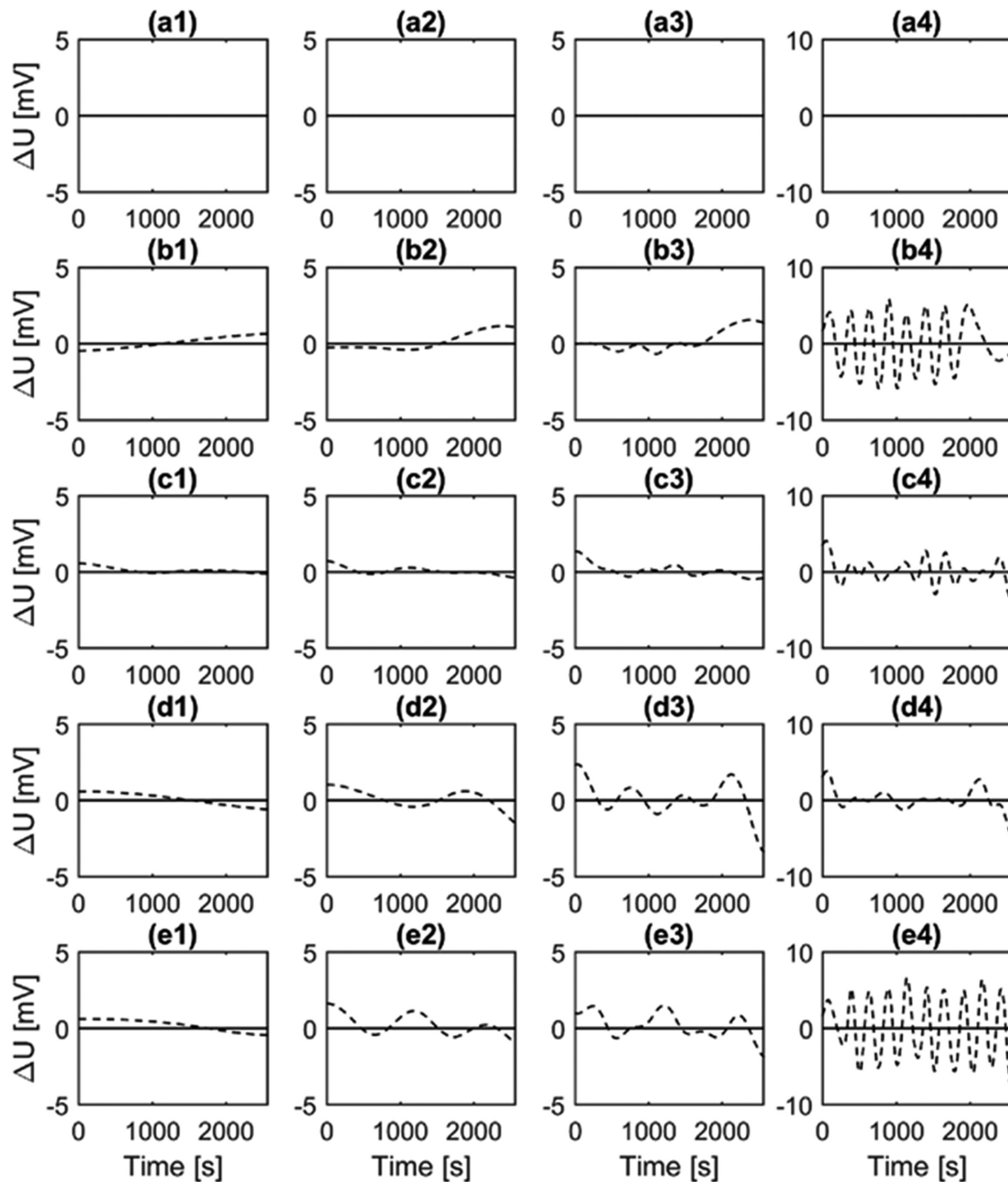
Figure 9. Comparisons of the real trend (solid line) and the fitting trend (dotted line) using different methods, when the original data are not contaminated by trend drift interference. (a1)–(a4) show the same figure, representing the trend obtained by the modified EMD method and the real trend term, which have completely overlapped. (b1)–(b4) show the fitting trends using the EMD method: in (b1), the dotted line is the residue; in (b2), the dotted line is the sum of the residue and the last IMF; in (b3), the dotted line is the sum of the residue and the last two IMFs; in (b4), the dotted line is the sum of the residue and the last three IMFs. (c1)–(c4) show the fitting trends using the EEMD method, (d1)–(d4) show the fitting trends using the CEEMD method, (e1)–(e4) show the fitting trends using ICEEMD method, and the subfigures in each column represent the sum of the different components.

contaminated by trend drift, background noise and burst noise interference. Through comparing Fig. 10(a) with Figs 10(b)–(d), the proposed method is still superior to the conventional methods.

Finally, we compare the computational costs of different methods using the three data models as shown in Table 1. All the calculations are done on an Intel core i5 processor at 2.50 GHz. The length of all three data sets is 163840. From modified EMD to EMD, EEMD, CEEMD and ICEEMD, the calculation cost increases gradually. The modified method is the most efficient in detrended item processing. This is because traditional methods require to compute multiple IMFs, and each IMF requires multiple iterations. If each IMF solution requires n iterations on average, $m \times n$ iterations are needed for m IMFs. However, for the modified method, the number of iterations needed is only equivalent to an IMF calculation.
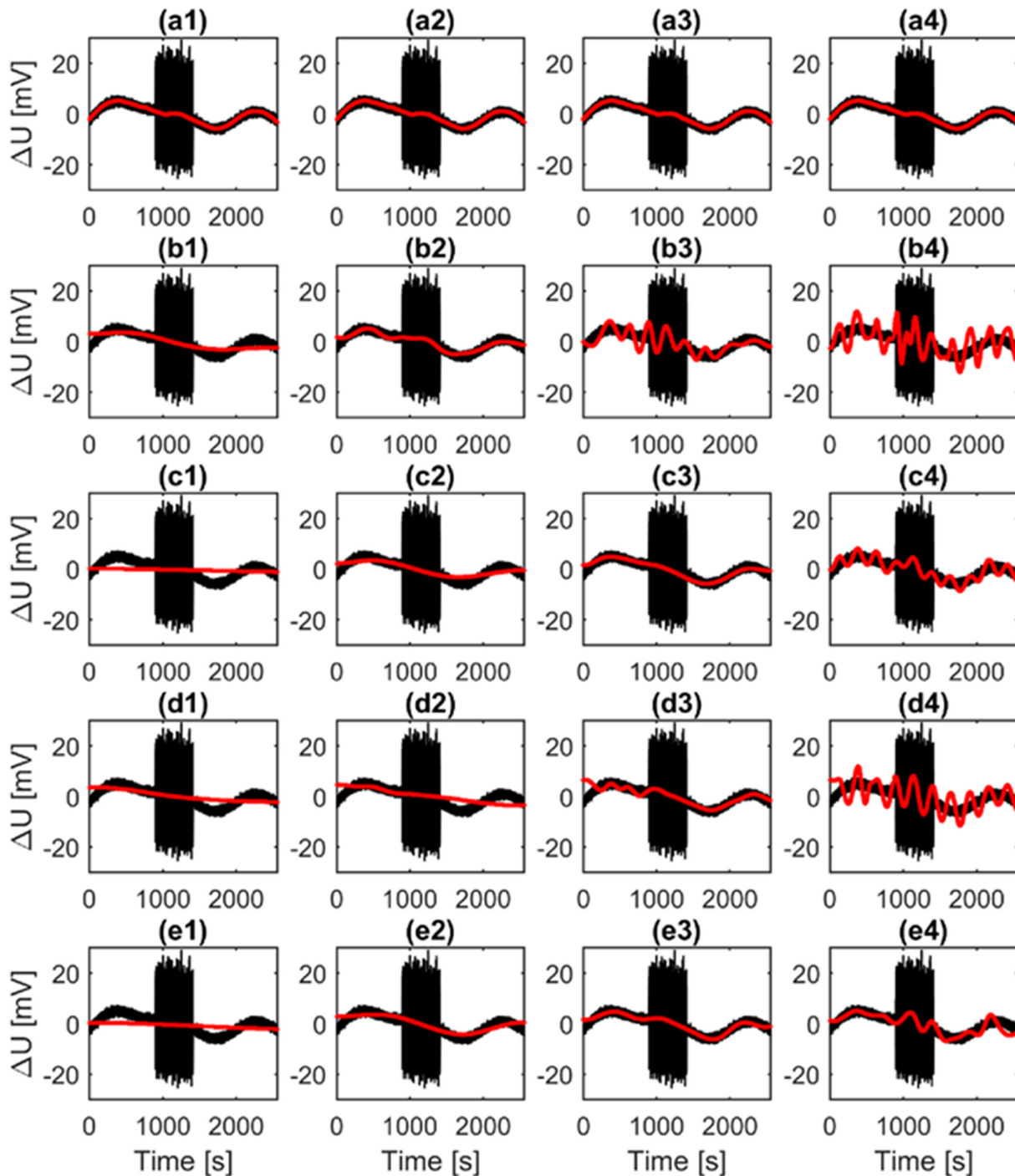
Figure 10. Comparisons of the real trend (solid line) and the fitting trend (dotted line) using different methods, when the original data are contaminated by sinusoidal trend drift, random noise and impulse noise interference. (a1)–(a4) show the same figure, representing the trend obtained by the modified EMD method and the real trend term, which have completely overlapped. (b1)–(b4) show the fitting trends using the EMD method: in (b1), the dotted line is the residue; in (b2), the dotted line is the sum of the residue and the last IMF; in (b3), the dotted line is the sum of the residue and the last two IMFs; in (b4), the dotted line is the sum of the residue and the last three IMFs. (c1)–(c4) show the fitting trends using the EEMD method, (d1)–(d4) show the fitting trends using the CEEMD method, and (e1)–(e4) show the fitting trends using the ICEEMD method.

Table 1. Comparisons of computational costs of various detrending methods (modified EMD, EMD, EEMD, CEEMD and ICEEMD) using three multiperiod time sequence models.

Method Computational costs (s)	Modified EMD	EMD	EEMD	CEEMD	ICEEMD
Model 1	0.92	11.06	69.79	154.88	124.48
Model 2	1.64	12.70	71.75	144.81	125.27
Model 3	0.87	15.69	70.32	135.38	138.41
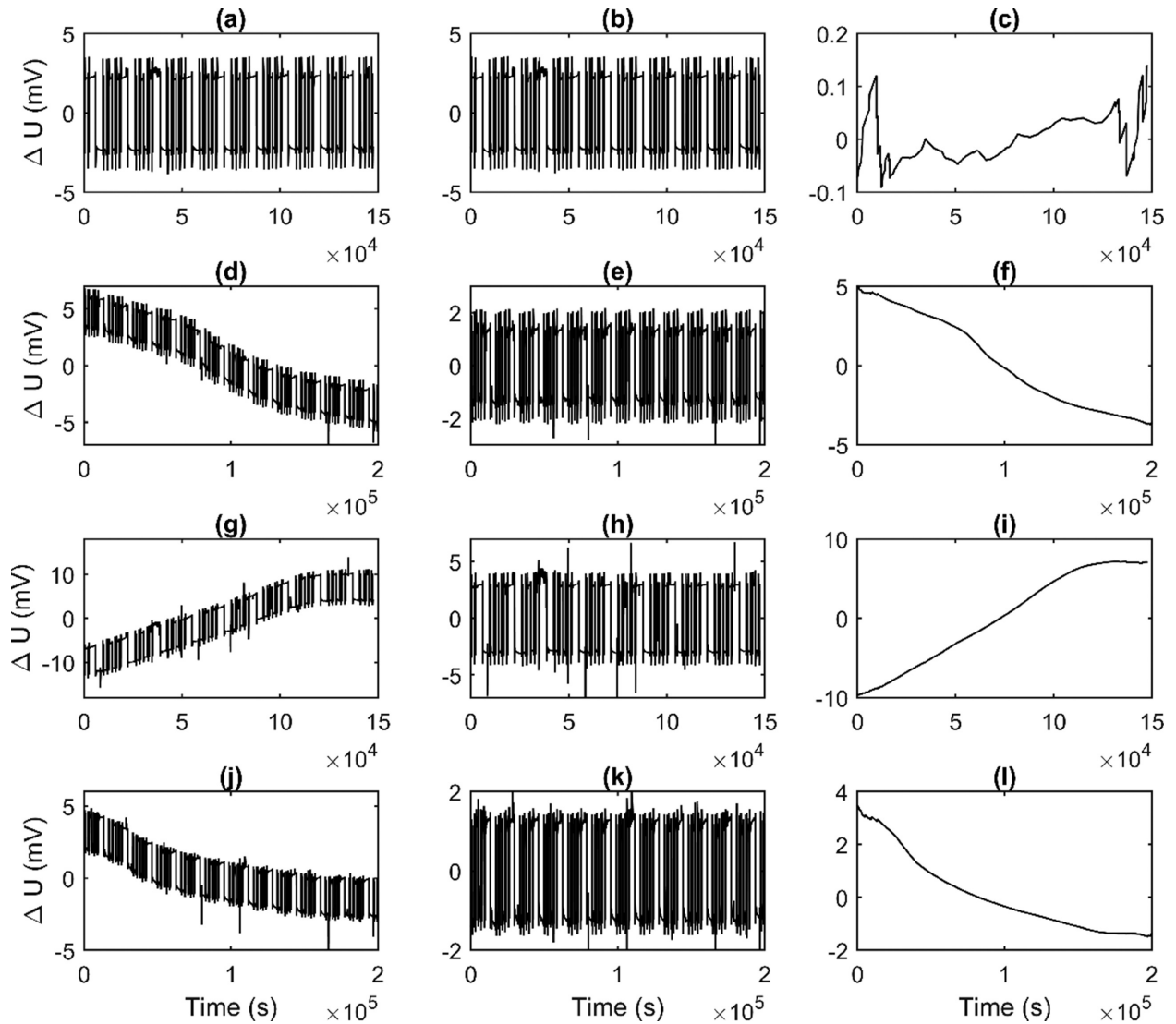
Figure 11. Using modified EMD to extract IP signal from raw data contaminated by practical trend interferences. Data of the left-hand column were the original IP signal, data of the median column were the extracted IP data and data of the right-hand column were the separated trend interference.

From the comparisons in Figs 8–10 and Table 1, we find that the modified EMD method can obtain a more accurate fitting trend, and the computational cost is only a fraction of the conventional EMD methods. It is, therefore, suitable for multiperiod signal detrending. However, it should be noted that this method is not applicable when the original signal is not a multiperiod signal. In addition, this method is only suitable for detrending, not for multiscale decomposition and reconstruction of signals. The method in this paper cannot completely replace the traditional method.

3.3 Comparison of the complex resistivity using IP data with and without tend drifting

To further investigate whether the modified EMD method will bring in additional phase shift and amplitude shift to the high-quality data, we use IP potential data with and without trend drifting to analyse the processing effect. Fig. 11 shows the separation of IP signal and practical trend interferences using the modified EMD method. Comparing Figs 11(a) and (b), we find that when the practical data are free of trend drifting, no significant change exists in the IP signals before and after processing. Figs 11(d), (g) & (j) and (e), (h) & (k) imply that when the trend is strong, the pure IP signal can be effectively separated from the interference.

Then, we use these IP potential data in Fig. 11 and their synchronous current data to calculate the complex resistivity by formula (1). In this survey area, potential difference and supplying current data of more than 10 periods are acquired. First, the original potential and current data are divided into two groups, including 1–5 periods and 6–10 periods. Then we use one method to process the two groups of data and calculate the apparent complex resistivity, respectively. Assume that ρ_1 and φ_1 are the apparent resistivity and phase calculated using the 1–5 periods data, and ρ_2 and φ_2 are the results calculated using the 6–10 periods data. The error between the two data are used to show the
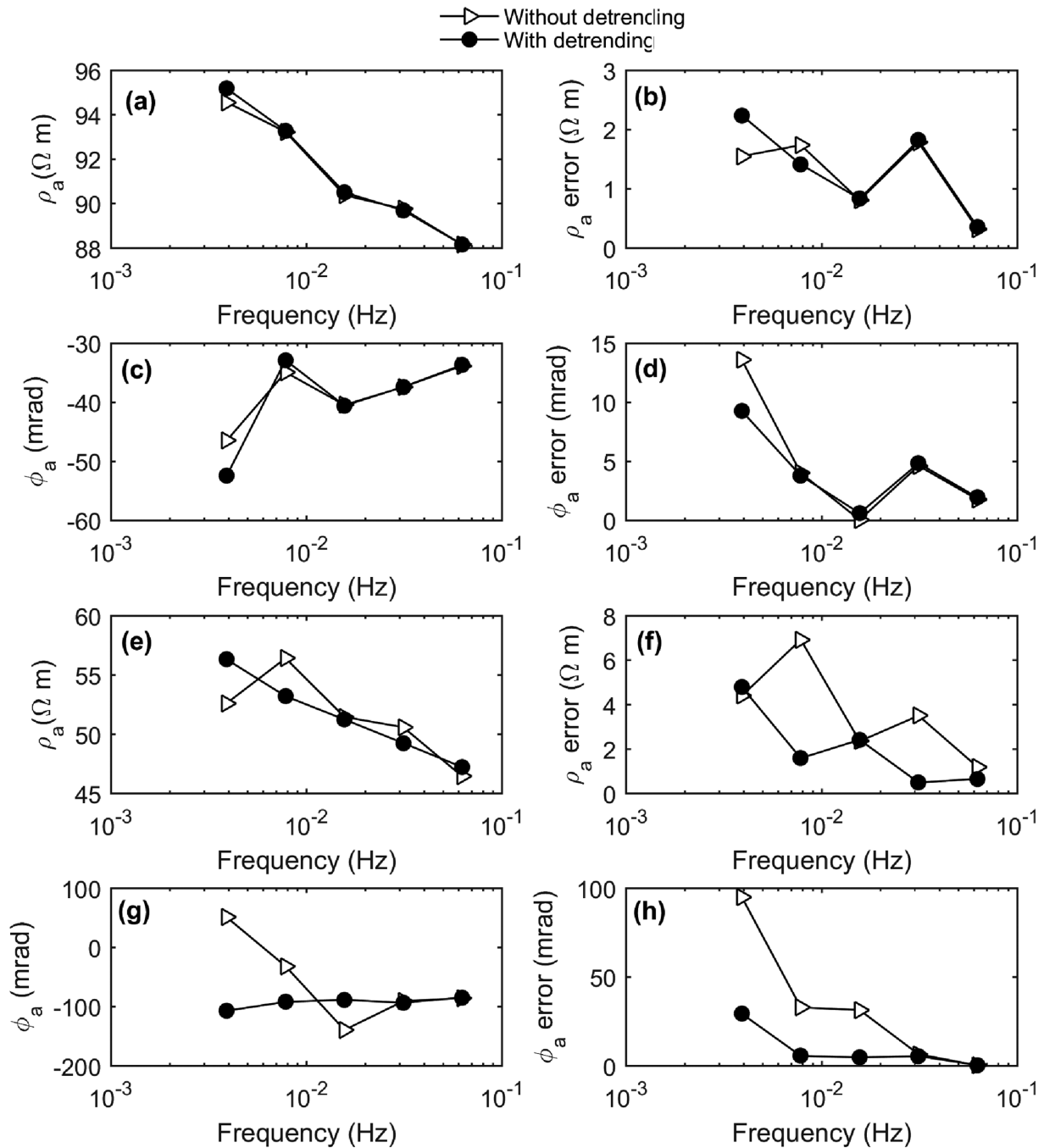
Figure 12. Apparent resistivity, apparent phase, resistivity error and phase error calculated with and without using the EMD processing for high-quality IP data (a–d) and low-quality IP data (e–h). (a) apparent resistivity of high-quality IP data; (b) apparent phase of high-quality IP data; (c) calculation error of apparent resistivity of high-quality IP data; (d) calculation error of apparent phase of high-quality IP data; (e) apparent resistivity of low-quality IP data; (f) apparent phase of low-quality IP data; (g) calculation error of apparent resistivity of low-quality IP data; (h) calculation error of apparent phase of low-quality IP data.

computation of error, which can be expressed as

$$\varepsilon_\rho = |\rho_1 - \rho_2| \text{ and } \varepsilon_\varphi = |\varphi_1 - \varphi_2|, \tag{13}$$

where ε_ρ and ε_φ are errors of apparent resistivity and phase. We took $(\rho_1 + \rho_2)/2$ and $(\varphi_1 + \varphi_2)/2$ as the final calculated apparent parameters.

First, we use IP potential data in Fig. 11(a) to calculate apparent parameters and error. Figs 12(a)–(d) show the results and errors with and without detrending. From Figs 12(a) and (c), there is no obvious phase shift and amplitude shift after detrending. From Figs 12(b) and (d), the range of resistivity error increases a little bit, and the phase error decreases slightly after detrending. Both the change of apparent resistivity and phase can be ignored overall. Then, the potential data in Fig. 11(j) and the synchronous current data are used to calculate the apparent complex resistivity with and without using the modified EMD processing. The results and errors are shown in Figs 12(e)–(h). Before
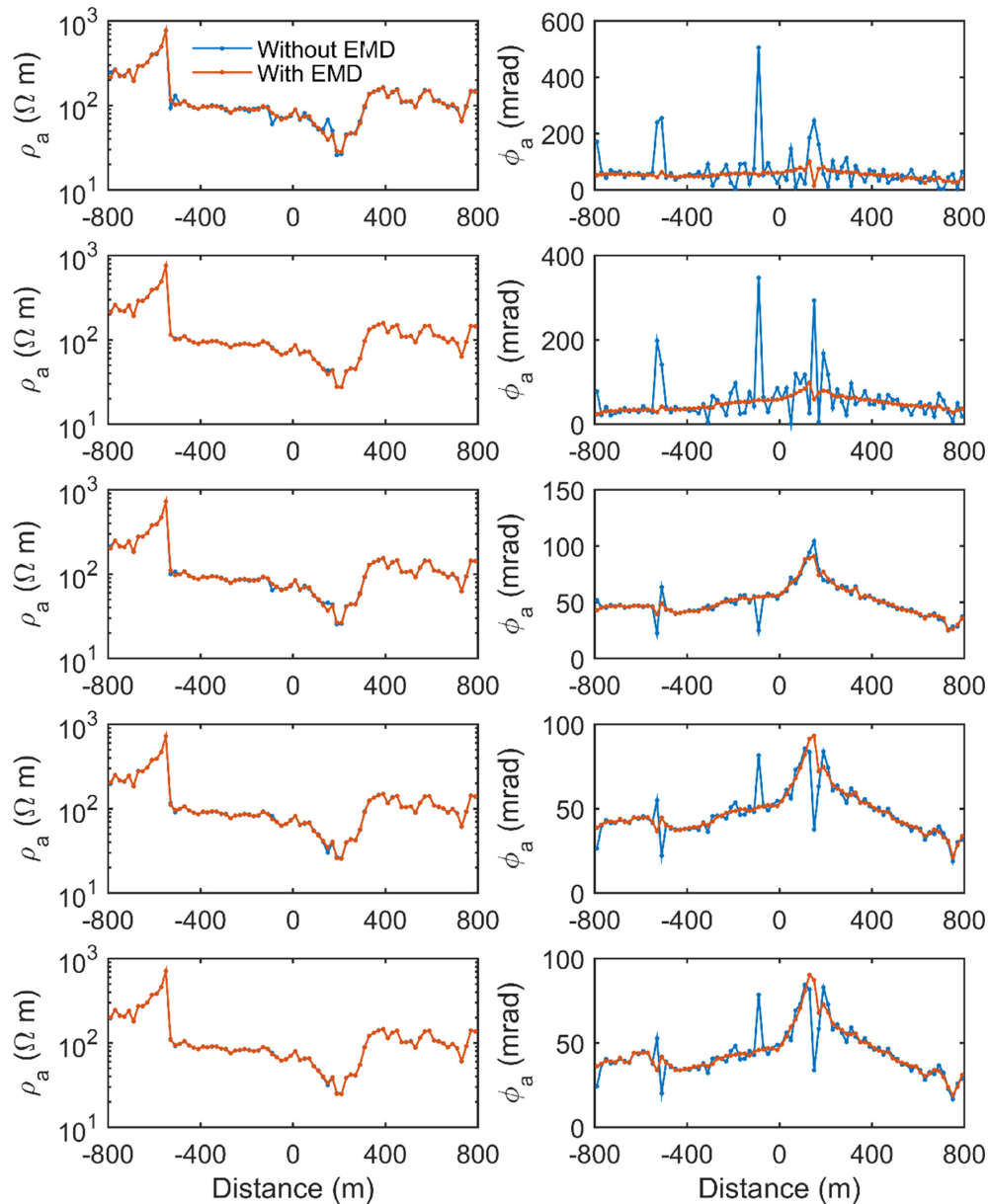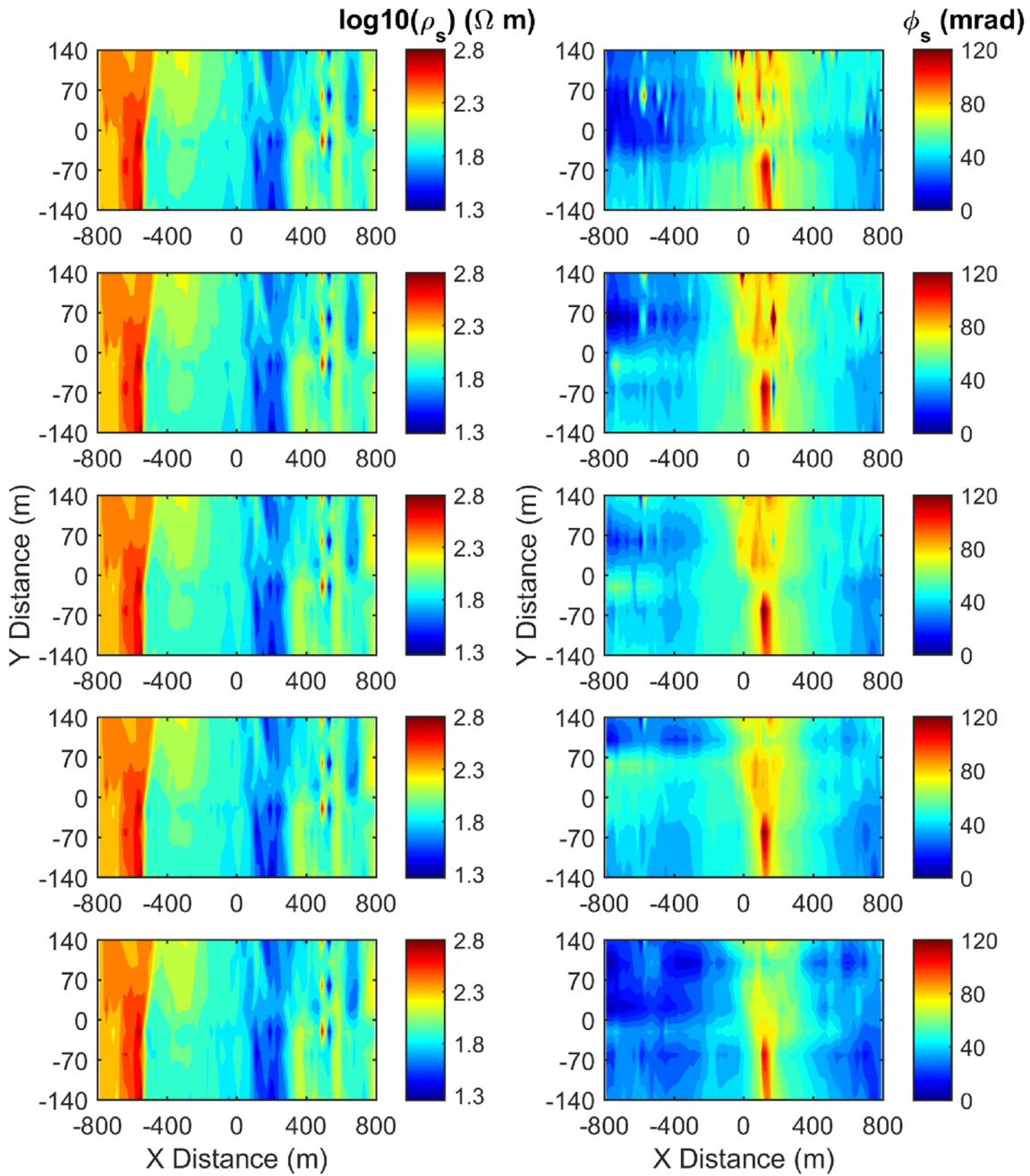
Figure 13. Apparent resistivity and phase profiles at five frequencies with and without the modified EMD processing. The left-hand column is the apparent resistivity with and without the modified EMD processing. The right-hand column is the apparent phase at the five frequencies with and without the modified EMD processing. From top to bottom, the frequencies are 0.0039, 0.0078, 0.0156, 0.0313 and 0.0625 Hz, respectively.

using EMD, both apparent resistivity and phase spectrum are rough. The resistivity error is 1–7 Ωm, and the largest phase error is nearly 100 mrad. After EMD processing, both resistivity and phase spectrum are smooth. The resistivity error is 0–4 Ωm, and the largest phase error is about 20 mrad. The results show that our proposed method can be used to improve the quality of IP data sets without causing additional phase shift or amplitude shift for the high-quality data.

4 COMPARISONS OF PRACTICAL LARGE-SCALE INDUCED POLARIZATION DATA PROCESSING WITH AND WITHOUT USING THE MODIFIED EMD METHOD

## 4.1 Comparisons of processed results for a survey line

To further test the effectiveness of the EMD method, we used the IP data of one survey line with and without EMD processing to calculate the apparent complex resistivity. The survey line is 1600 m long and arranged using intermediate gradient array protocol. The current electrode space AB/2 is 2500 m. Both the survey point space and potential electrode space are 20 m. Supplying current and 80-channel potential data were acquired synchronously. After the completion of data collection, for each survey point, first, we calculated complex resistivity at five

Figure 14. The plane contour maps of the apparent resistivity (the left-hand column) and phase (the right-hand column) at five frequencies by using the modified EMD processing (from top to bottom: 0.0039, 0.0078, 0.0156, 0.0313 and 0.0625 Hz).

frequencies using current data and potential data after general correction using conventional polynomial fitting methods. Then, we used the modified EMD method to separate the IP potential data and trend drift interference. Detrending data were used to calculate the complex resistivity. The left-hand column in Fig. 13 shows the apparent resistivity profiles for this survey line with and without EMD processing; from top to bottom, the frequencies are 0.0039, 0.0078, 0.0156, 0.0313 and 0.0625 Hz, respectively. The right-hand column in Fig. 13 shows the apparent phase profiles for this survey line with and without EMD processing.

As shown in Fig. 13, there is a little change in apparent resistivity with and without EMD processing. However, there is a huge change in apparent phase. Before detrending, the phase profiles are rough and there are many outliers, especially for the results at 0.0039 and 0.0078 Hz. After detrending, the profiles are smooth and reasonable, and the outliers disappear. As shown in Fig. 13, there is an anomalous body with high phase and low resistivity from distances 100 to 200 m, which can be used for the location forecasting of the buried ore body.
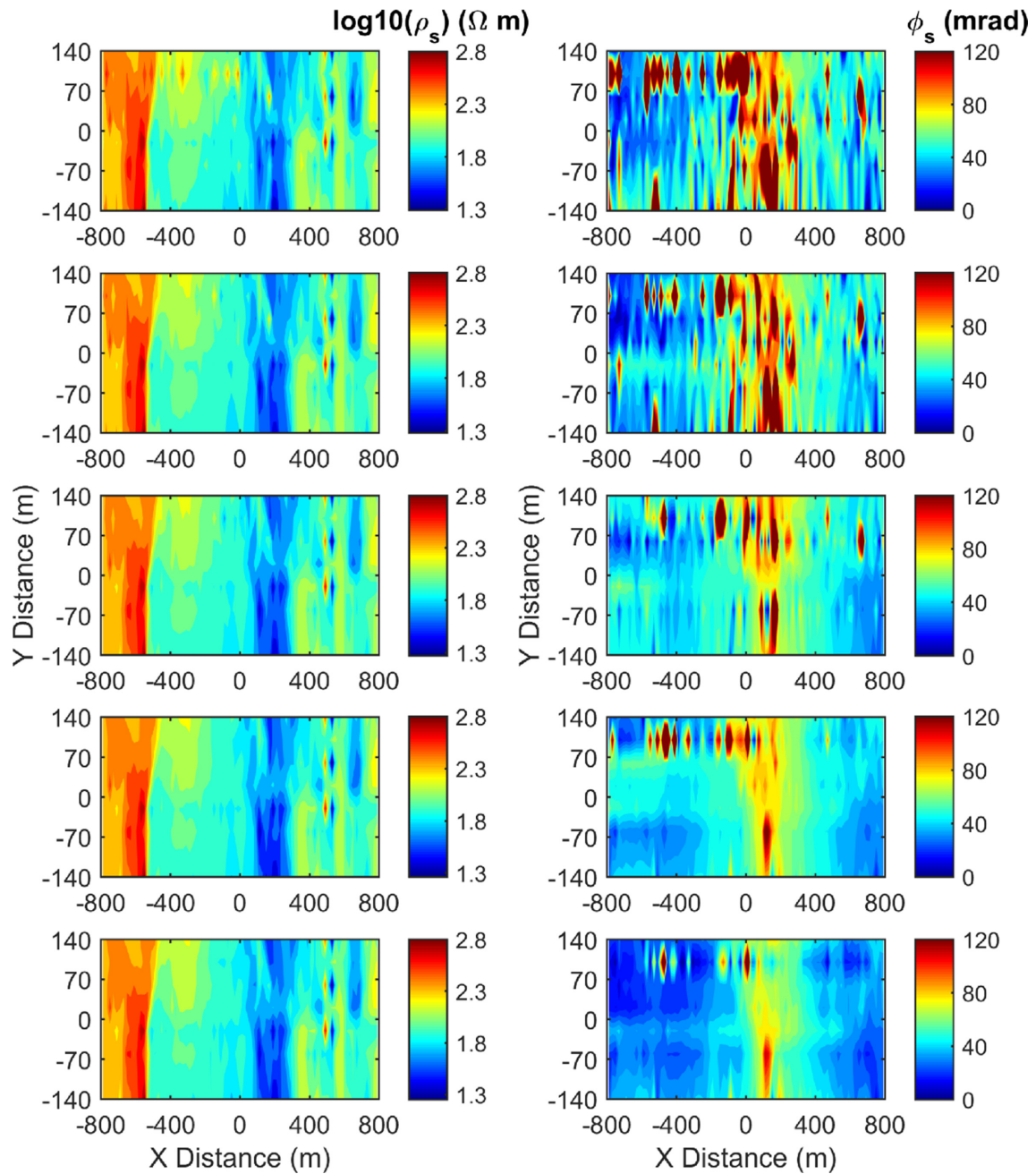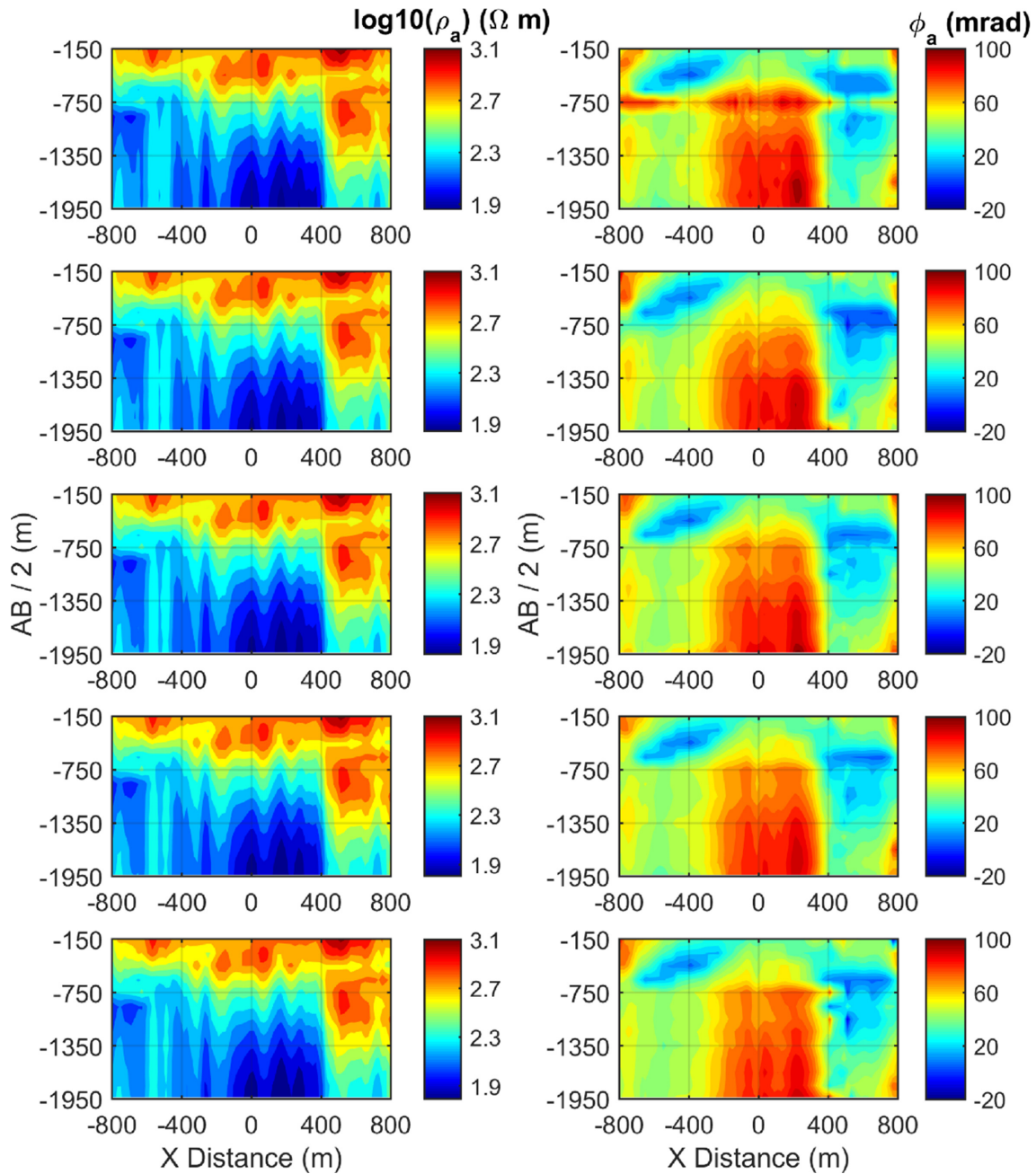
Figure 15. The plane contour maps of the apparent resistivity (the left-hand column) and phase (the right-hand column) at five frequencies without using the modified EMD processing (from top to bottom: 0.0039, 0.0078, 0.0156, 0.0313 and 0.0625 Hz).

4.2 Comparisons of processed results for a contour map

To further validate the apparent complex resistivity and phase calculated using the modified EMD method, we applied this processing to IP data of multiple survey lines using intermediate gradient array protocol. The apparent complex resistivity and phase contour maps were plotted. Fig. 14 shows the contour maps of the apparent complex resistivity and phase at five frequencies using the modified EMD processing respectively. Fig. 15 shows these contour maps of the apparent phase and phase without using the processing respectively. Both in Figs 14 and 15, from top to bottom, the frequencies are 0.0039, 0.0078, 0.0156, 0.0313 and 0.0625 Hz, respectively. Apparent resistivity shows very similar plane contour maps using and without using the modified EMD processing; however, there is a remarkable improvement with much smoother contour maps and higher anomalies for the apparent phase by EMD processing in Fig. 14. Through comparison, the influence of trend interference is very large at low frequencies (0.0039, 0.0078 and 0.0156 Hz) and small at high frequencies (0.0313 and 0.0625 Hz). In Fig. 14, IP data of these survey lines revealed that high-phase anomaly conforms with low-resistivity anomaly on 100–300 m; additionally, a high resistivity with low phase anomaly was revealed on −700 to –500 m.
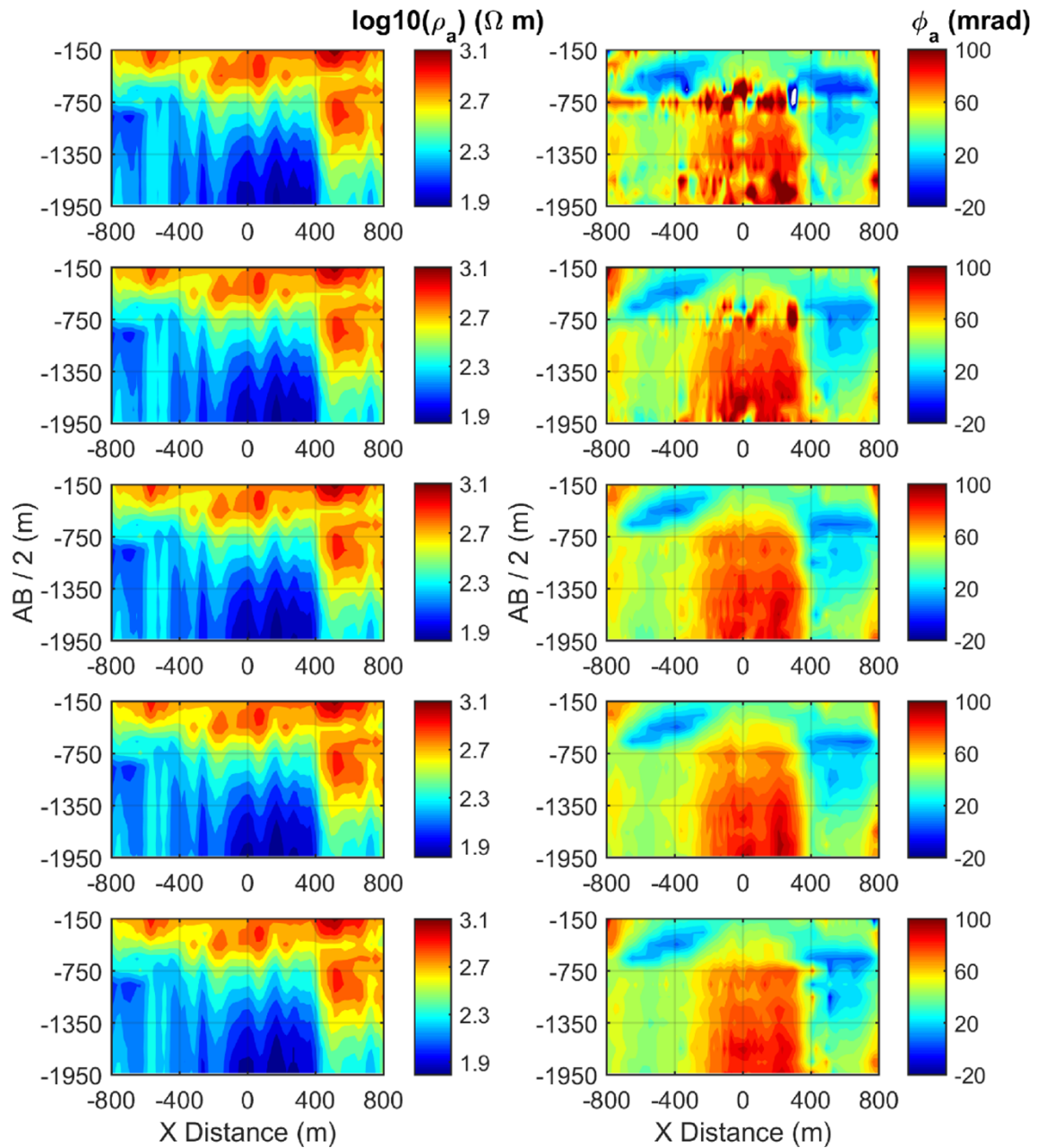
Figure 16. The pseudo-sections of the apparent resistivity (the left-hand column) and phase (the right-hand column) at five frequencies by using the modified EMD processing (from top to bottom: 0.0039, 0.0078, 0.0156, 0.0313 and 0.0625 Hz).

4.3 Comparisons of processed results for a pseudo-section

Then, we applied this processing method to IP data of non-conventional sounding device. The survey line is 1600 m long. Both the survey point space and potential electrode space are 20 m, and the current electrode space AB/2 is 150, 300, 450, 600, 750, 900, 1050, 1200, 1350, 1500, 1650, 1800 and 1950 m, respectively. Figs 16 and 17 show the pseudo-sections with and without the modified EMD processing. Through comparison, we found that the pseudo-sections of apparent resistivity are almost the same before and after EMD processing. The pseudo-sections of apparent phase changed a lot after processing, especially at the low frequency ($f = 00039$ Hz and $f = 0.0078$ Hz). Before processing, due to the existence of the outliers, the target body's abnormality is suppressed. After processing, the outlier disappears, and the deep anomaly is highlighted. A low-resistivity and high-phase anomaly was also found in 0–400 m. The anomalies will be inversed and interpreted combined with other geological data in the future.

Overall, the influence of low-frequency trend interference on the apparent phase is stronger than that on the apparent resistivity. This is because the resistivity is determined by the total potential (the sum of primary potential and secondary potential), which is strong. However, phase of the potential and current is determined by the secondary potential, which is weak. Additionally, when the frequency is low and the

Figure 17. The pseudo-sections of the apparent resistivity (the left-hand column) and phase (the right-hand column) at five frequencies without using the modified EMD processing (from top to bottom: 0.0039, 0.0078, 0.0156, 0.0313 and 0.0625 Hz).

current electrode space is large, the influence of trend interference is increasing because the SNR is reduced. The EMD method is necessary for the deep SIP exploration, when the electrode distance AB is large and the frequency is low.

5 CONCLUSION AND DISCUSSION

A modified EMD detrending method is developed to filter the IP data contaminated by low-frequency trend interference. Through comparing with the traditional empirical mode methods, testing the IP data with simulated and practical interference, and analysing the complex resistivity profiles before and after detrending, the following conclusions can be drawn: The modified EMD method with low computational costs and strong anti-interference capability can obtain a more accurate fitting trend drift than conventional EMD methods. The quality of complex resistivity data can be improved by detrending the IP time-series, and full profiles of apparent parameters are smooth and reasonable after processing. Overall, the modified EMD method can improve multiperiod full-waveform IP data reliability and quality to advance the application of large-scale distributed IP exploration.

In recent years, many new signal processing methods have also been proposed and applied in geophysical signal processing, including MMF, EWT, VMD, EMD-seislet transform and so on. Due to limited space, this paper does not compare the above methods and the proposed modified EMD method in detail. For MMF, a suitable structural element function for IP signal is needed to be developed. For EWT, VMD and EMD-seislet, the computational cost needs to be further reduced for large-scale data processing. The application of the above methods in the detrending of IP multiperiod time-series should be researched in the future.

ACKNOWLEDGEMENTS

REFERENCES

Battista, B.M., Knapp, C., McGee, T. & Goebel, V., 2007. Application of the empirical mode decomposition and Hilbert-Huang transform to seismic reflection data, *Geophysics,* **72**(2), 29–37.

Bekara, M. & Van der Baan, M., 2009. Random and coherent noise attenuation by empirical mode decomposition, *Geophysics,* **74**(5), 89–98.

Belliveau, P. & Haber, E., 2018. Coupled simulation of electromagnetic induction and induced polarization effects using stretched exponential relaxation, *Geophysics,* **83**(2), WB109–WB121.

Bhattacharya, P.K. & Patra, H.P., 1968. *Direct Current Geoelectric Sounding: Principles and Interpretation,* Methods in Geochemistry and Geophysics, Elsevier.

Bleil, D.F., 1953. Induced polarisation: a method of geophysical prospecting, *Geophysics,* **18**(3), 636–661.

Cai, J., Tang, J., Hua, X. & Gong, Y., 2009. An analysis method for magnetotelluric data based on the Hilbert–Huang transform, *Explor. Geophys.,* **40**(2), 197–205.

Chen, C., Wang, C., Liu, J., Liu, C., Liang, W., Yen, H. & Wang, Y., 2010. Identification of earthquake signals from groundwater level records using the HHT method, *Geophys. J. Int.,* **180**(3), 1231–1241.

Chen, J., Heincke, B., Jegen, M. & Moorkamp, M., 2012. Using empirical mode decomposition to process marine magnetotelluric data, *Geophys. J. Int.,* **190**(1), 293–309.

Chen, R., Luo, W. & He, J., 2007. High precision multi-frequency multi-function receiver for electrical exploration, in *2007 8th International Conference on Electronic Measurement and Instruments, IEEE, Expanded Abstracts,* Xi'an, China, pp. 600–602.

Chen, W., Chen, Y. & Liu, W., 2016. Ground roll attenuation using improved complete ensemble empirical mode decomposition, *J. Seismic Explor.,* **25**(5), 485–495.

Chen, W., Xie, J., Zu, S., Gan, S. & Chen, Y., 2017a. Multiple-reflection noise attenuation using adaptive randomized-order empirical mode decomposition, *IEEE Geosci. Remote Sens. Lett.,* **14**(1), 18–22.

Chen, W., Zhang, D. & Chen, Y., 2017b. Random noise reduction using a hybrid method based on ensemble empirical mode decomposition, *J. Seismic Explor.*, **26**(3), 227–249.

Chen, Y., 2016. Dip-separated structural filtering using seislet transform and adaptive empirical mode decomposition based DIP filter, *Geophys. J. Int.,* **206**(1), 457–469.

Chen, Y. & Fomel, S., 2017. EMD-seislet transform, *Geophysics,* **83**(1), A27–A32.

Chen, Y. & Ma, J., 2014. Random noise attenuation by *f–x* empirical-mode decomposition predictive filtering, *Geophysics,* **79**(3), V81–V91.

Chen, Y., Zhang, G., Gan, S. & Zhang, C., 2015. Enhancing seismic reflections using empirical mode decomposition in the flattened domain, *J. Appl. Geophys.,* **119,** 99–105.

Colominas, M.A., Schlotthauer, G. & Torres, M.E., 2014. Improved complete ensemble EMD: a suitable tool for biomedical signal processing, *Biomed. Signal Process. Control,* **14,** 19–29.

Commer, M., Petrov, P.V. & Newman, G.A., 2017. FDTD modelling of induced polarization phenomena in transient electromagnetics, *Geophys. J. Int.,* **209**(1), 387–405.

Dahlin, T., Leroux, V. & Nissen, J., 2002. Measuring techniques in induced polarisation imaging, *J. Appl. Geophys.,* **50**(3), 279–298.

Deo, R.N. & Cull, J.P., 2015. Denoising time-domain induced polarization data using wavelet techniques, *Explor. Geophys.,* **47**(2), 108–114.

Dey, A. & Morrison, H.F., 1973. Electromagnetic coupling in frequency and time-domain induced-polarization surveys over a multilayered earth, *Geophysics,* **38**(2), 380–405.

Dragomiretskiy, K. & Zosso, D., 2014. Variational mode decomposition, *IEEE Trans. Signal Process.,* **62**(3), 531–544.

Eaton, P, Anderson, B., Queen, S., Mackenzie, I. & Wynn, D., 2010. NEWDAS—The Newmont distributed IP data acquisition system, in *80th Annual International Meeting, SEG, Expanded Abstracts,* pp. 1768–1772, doi:10.1190/1.3513184.

Fiandaca, G., Madsen, L.M. & Maurya, P.K., 2018. Re-parameterisations of the Cole-Cole model for improved spectral inversion of induced polarization data, *Near Surf. Geophys.,* **16**(4), 385–399.

Flandrin, P., Goncalves, P. & Rilling, G., 2004. Detrending and denoising with empirical mode decompositions, in *12th European Signal Processing Conference,* IEEE, Vienna, Austria, pp. 1581–1584.

Gharibi, M., Killin, K., McGill, D., Henderson, W.B. & Retallick, T., 2012. Full 3D acquisition and modelling with the quantec 3D system-the hidden hill deposit case study, *ASEG Extended Abstracts,* **2012**(1), 1–4.

Gilles, J., 2013. Empirical wavelet transform, *IEEE Trans. Signal Process.,* **61**(16), 3999–4010.

Golomb, S.W., 1982. *Shift Register Sequences,* Aegean Park Press.

Gourry, J.C., Vermeersch, F., Garcin, M. & Giot, D., 2003. Contribution of geophysics to the study of alluvial deposits: a case study in the Val d' Avaray area of the River Loire, France, *J. Appl. Geophys.,* **54**(1-2), 35–49.

Han, J. & van der Baan, M., 2013. Empirical mode decomposition for seismic time-frequency analysis, *Geophysics,* **78**(2), 9–19.

Han, J. & van der Baan, M., 2015. Microseismic and seismic denoising via ensemble empirical mode decomposition and adaptive thresholding, *Geophysics,* **80**(6), 69–80.

Hassan, H.H., 2005. Empirical mode decomposition (EMD) of potential field data: airborne gravity data as an example, in *75th Annual International Meeting, SEG, Expanded Abstracts,* pp. 704–706, doi:10.1190/1.2144422.

He, J., 1997. Frequency domain electrical methods employing special wave form field sources, in *67th Annual Meetin, SEG, Expanded Abstracts,* pp. 338–341.

He, J., Yang, Y., Li, D. & W, J., 2015. Wide field electromagnetic sounding methods, in *Symposium on the Application of Geophysics to Engineering and Environmental Problems (SAGEEP 2015), EEGS, Expanded Abstracts,* pp. 325–329, doi:10.4133/SAGEEP.28-047.

Huang, J., Zhao, B., Chen, Y. & Zhao, P., 2010. Bidimensional empirical mode decomposition (BEMD) for extraction of gravity anomalies associated with gold mineralization in the Tongshi gold field, Western Shandong Uplifted Block, Eastern China, *Comput. Geosci.,* **36**(7), 987–995.

Huang, N. *et al.*, 1998. The empirical mode decomposition and the Hilbert spectrum for nonlinear and non-stationary time series analysis, *Proc. R. Soc. A,* **454**(1998), 903–995.

Huang, W., Wang, R., Zu, S. & Chen, Y. 2017. Low-frequency noise attenuation in seismic and microseismic data using mathematical morphological filtering. *Geophys. J. Int.,* **211**(3), 1318–1340.

Jackson, L.P. & Mound, J.E., 2010. Geomagnetic variation on decadal time scales: what can we learn from empirical mode decomposition? *Geophys. Res. Lett.,* **37**(14), 1–6.

Jeng, Y., Lin, M., Chen, C. & Wang, Y., 2007. Noise reduction and data recovery for a VLF-EM survey using a nonlinear decomposition method. *Geophysics,* **72**(5), 223–235.

Johnson, I.M., 1984. Spectral induced polarization parameters as determined through time-domain measurements. *Geophysics,* **49**(11), 1993–2003.

Karaoulis, M., Revil, A., Tsourlos, P., Werkema, D.D. & Minsley, B.J., 2013. IP4DI: a software for time-lapse 2D/3D DC-resistivity and induced polarization tomography, *Comput. Geosci.,* **54**, 164–170.

Kim, B., Nam, M.J. & Kim, H.J., 2018. Inversion of time-domain induced polarization data based on time-lapse concept, *J. Appl. Geophys.,* **152**, 26–37.

Larsen, J.J., Dalgaard, E. & Auken, E., 2013. Noise cancelling of MRS signals combining model-based removal of powerline harmonics and multichannel Wiener filtering, *Geophys. J. Int.,* **196**(2), 828–836.

Li, G., Xiao, X., Tang, J.T., Li, J., Zhu, H.J., Zhou, C. & Yan, F.B., 2017. Near-source noise suppression of AMT by compressive sensing and mathematical morphology filtering, *Appl. Geophys.,* **14**(4), 581–589.

Li, H., Wang, R., Cao, S., Chen, Y. & Huang, W., 2016. A method for low-frequency noise suppression based on mathematical morphology in microseismic monitoring, *Geophysics,* **81**(3), V159–V167.

Li, Y. & Oldenburg, D.W., 2000. 3-D inversion of induced polarization data, *Geophysics,* **65**(6), 1931–1945.

Liu, W., Cao, S. & Chen, Y., 2016a. Applications of variational mode decomposition in seismic time-frequency analysis, *Geophysics,* **81**(5), V365–V378.

Liu, W., Cao, S. & Chen, Y., 2016b. Seismic time-frequency analysis via empirical wavelet transform, *IEEE Geosci. Remote Sens. Lett.,* **13**(1), 28–32.

Liu, W., Chen, R., Cai, H. & Luo, W., 2016c. Robust statistical methods for impulse noise suppressing of spread spectrum induced polarization data, with application to a mine site, Gansu province, China, *J. Appl. Geophys,* **135**, 397–407.

Liu, W., Chen, R., Cai, H., Luo, W. & Revil, A., 2017. Correlation analysis for spread-spectrum induced-polarization signal processing in electromagnetically noisy environments, *Geophysics,* **82**(5), E243–E256.

Mary, B., Saracco, G., Peyras, L., Vennetier, M., Mériaux, P. & Camerlynck, C., 2016. Mapping tree root system in dikes using induced polarization: focus on the influence of soil water content, *J. Appl. Geophys.,* **135**, 387–396.

Maurya, P.K., Balbarini, N., Møller, I., Rønde, V., Christiansen, A.V., Bjerg, P.L., Auken, E. & Fiandaca, G., 2018. Subsurface imaging of water electrical conductivity, hydraulic permeability and lithology at contaminated sites by induced polarization, *Geophys. J. Int.,* **213**(2), 770–785.

Mo, D., Jiang, Q., Li, D., Chen, C., Zhang, B. & Liu, J., 2017. Controlled-source electromagnetic data processing based on gray system theory and robust estimation, *Appl. Geophys.,* **14**, 570–580.

Nabighian, M.N. & Macnae, J.C., 1991. Time domain electromagnetic prospecting methods, *Electromagn. Methods Appl. Geophys.,* **2**(part A), 427–509.

Olsson, P.I., Dahlin, T., Fiandaca, G. & Auken, E., 2015. Measuring time-domain spectral induced polarization in the on-time: decreasing acquisition time and increasing signal-to-noise ratio, *J. Appl. Geophys.,* **123**, 316–321.

Olsson, P.I., Fiandaca, G., Larsen, J.J., Dahlin, T. & Auken, E., 2016. Doubling the spectrum of time-domain induced polarization by harmonic de-noising, drift correction, spike removal, tapered gating and data uncertainty estimation, *Geophys. J. Int.,* **207**(2), 774–784.

Oppenheim, A.V., 1989. *Discrete-Time Signal Processing,* Pearson Education India.

Peter-Borie, M., Sirieix, C., Naudet, V. & Riss, J., 2011. Electrical resistivity monitoring with buried electrodes and cables: noise estimation with repeatability tests, *Near Surf. Geophys.,* **9**(4), 369–380.

Power, C., Tsourlos, P., Ramasamy, M., Nivorlis, A. & Mkandawire, M., 2018. Combined DC resistivity and induced polarization (DC-IP) for mapping the internal composition of a mine waste rock pile in Nova Scotia, Canada, *J. Appl. Geophys.,* **150**, 40–51.

Qi, Y., El-Kaliouby, H., Revil, A., Ahmed, A.S., Ghorbani, A. & Li, J., 2019. Three-dimensional modeling of frequency-and time-domain electromagnetic methods with induced polarization effects, *Comput. Geosci.,* **124**, 85–92.

Revil, A., Binley, A., Mejus, L. & Kessouri, P., 2015. Predicting permeability from the characteristic relaxation time and intrinsic formation factor of complex conductivity spectra, *Water Resour. Res.,* **51**(8), 6672–6700.

Routh, P.S. & Oldenburg, D.W., 2001. Electromagnetic coupling in frequency-domain induced polarization data: a method for removal, *Geophys. J. Int.,* **145**(1), 59–76.

Serra, J., 1986. Introduction to mathematical morphology, *Comput. Vis. Graph. Image Process.,* **35**(3), 283–305.

Shen, W.B. & Ding, H., 2014. Observation of spheroidal normal mode multiplets below 1 mHz using ensemble empirical mode decomposition, *Geophys. J. Int.,* **196**(3), 1631–1642.

Soueid Ahmed, A., Revil, A., Jardani, A. & Chen, R., 2018. 3D geostatistical inversion of induced polarization data and its application to coal seam fires, *Geophysics,* **83**(3), E133–E150.

Sun, J., Li, Y. & Nabighian, M., 2012. Lithology differentiation based on inversion of full waveform induced polarization data from Newmont Distributed IP Data Acquisition System (NEWDAS), in *82nd Annual International Meeting, SEG, Expanded Abstracts,* pp. 1–5, doi:10.1190/segam2012-1378.1.

Tavakoli, S., Bauer, T.E., Rasmussen, T.M., Weihed, P. & Elming, S.Å., 2016. Deep massive sulphide exploration using 2D and 3D geoelectrical and induced polarization data in Skellefte mining district, northern Sweden, *Geophys. Prospect.,* **64**(6), 1602–1619.

Torres, M.E., Colominas, M.A., Schlotthauer, G. & Flandrin, P., 2011. A complete ensemble empirical mode decomposition with adaptive noise, in *2011 IEEE International Conference on Acoustics, Speech and Signal Processing (ICASSP),* pp. 4144–4147, IEEE, Prague, Czech Republic.

Wait, J.R., 1959. The variable-frequency method, in *Overvoltage Research and Geophysical Applications,* Pergamon Press, pp. 29–49.

Wu, Z. & Huang, N.E., 2009. Ensemble empirical mode decomposition: a noise-assisted data analysis method, *Adv. Adapt. Data Anal.*, **1**(01), 1–41.

Xi, X., Yang, H., He, L. & Chen, R., 2013. Chromite mapping using induced polarization method based on spread spectrum technology, in *Symposium on the Application of Geophysics to Engineering and Environmental Problems (SAGEEP 2013), EEGS, Expanded Abstracts,* pp. 13–19, doi:10.4133/sageep2013-015.1.

Xi, X., Yang, H., Zhao, X., Yao, H., Qiu, J., Shen, R. & Chen, R., 2014. Large-scale distributed 2D/3D FDIP system based on ZigBee network and GPS, in *Symposium on the Application of Geophysics to Engineering and Environmental Problems (SAGEEP 2014), EEGS, Expanded Abstracts,* pp. 130–139, doi:10.4133/SAGEEP.27-055.

Xue, Y., Cao, J. & Tian, R., 2014. EMD and Teager–Kaiser energy applied to hydrocarbon detection in a carbonate reservoir, *Geophys. J. Int.,* **197**(1), 277–291.

Zhdanov, M., Endo, M., Cox, L. & Sunwall, D., 2018. Effective-medium inversion of induced polarization data for mineral exploration and mineral discrimination: Case study for the copper deposit in Mongolia, *Minerals,* **8**(68), 1–22.

Zonge, K.L. & Wynn, J.C., 1975. Recent advances and applications in complex resistivity measurements, *Geophysics,* **40**(5), 851–864.

Zonge, K.L., Wynn, J.C. & Urquhart, S., 2005. Resistivity, induced polarization, and complex resistivity, *Near Surf. Geophys.,* **9**, 265–300.